Monthly Notices of the ROYAL ASTRONOMICAL SOCIETY

MNRAS **546,** 1–28 (2026) https://doi.org/10.1093/mnras/stag094
Advance Access publication 2026 January 15

Exploring spatially resolved metallicities, dynamics, and outflows in low-mass galaxies at $z \sim 7.6$

L. R. Ivey [1,2★] J. Scholtz [1,2] A. L. Danhaive [1,2] S. Koudmani [1,3,4] G. C. Jones [1,2] R. Maiolino,[1,2,5] M. Curti,[6] F. D'Eugenio [1,2] S. Tacchella [1,2] W. M. Baker [7] S. Arribas,[8] S. Charlot [9] D. Eisenstein [10] Z. Ji,[11] M. Koller [1,2] N. Laporte,[12] M. Perna,[8] D. Puskás,[1,2] B. Robertson,[13] D. Sijacki,[1,14] J. A. A. Trussler[10] and C. Witten [15]

[1]*Kavli Institute for Cosmology, University of Cambridge, Madingley Road, Cambridge CB3 0HA, UK*
[2]*Cavendish Laboratory, University of Cambridge, 19 JJ Thomson Avenue, Cambridge CB3 0HE, UK*
[3]*St Catharine's College, University of Cambridge, Trumpington Street, Cambridge CB2 1RL, UK*
[4]*Centre for Astrophysics Research, Department of Physics, Astronomy and Mathematics, University of Hertfordshire, College Lane, Hatfield AL10 9AB, UK*
[5]*Department of Physics and Astronomy, University College London, Gower Street, London WC1E 6BT, UK*
[6]*European Southern Observatory, Karl-Schwarzschild-Strasse 2, D-85748 Garching, Germany*
[7]*DARK, Niels Bohr Institute, University of Copenhagen, Jagtvej 128, DK-2200 Copenhagen, Denmark*
[8]*Centro de Astrobiología (CAB), CSIC–INTA, Cra. de Ajalvir Km. 4, E-28850-Torrejón de Ardoz, Madrid, Spain*
[9]*Sorbonne Université, CNRS, UMR 7095, Institut d'Astrophysique de Paris, 98 bis bd Arago, F-75014 Paris, France*
[10]*Center for Astrophysics | Harvard & Smithsonian, 60 Garden St., Cambridge, MA 02138,USA*
[11]*Steward Observatory, University of Arizona, 933 N. Cherry Avenue, Tucson, AZ 85721, USA*
[12]*Aix Marseille Université, CNRS, CNES, LAM, Marseille, France*
[13]*Department of Astronomy and Astrophysics, University of California, Santa Cruz, 1156 High Street, Santa Cruz, CA 95064, USA*
[14]*Institute of Astronomy, University of Cambridge, Madingley Road, Cambridge, CB3 0HA, UK*
[15]*Department of Astronomy, University of Geneva, Chemin Pegasi 51, CH-1290 Versoix, Switzerland*

Accepted 2026 January 13. Received 2026 January 8; in original form 2025 July 20

ABSTRACT

A majority of *JWST*/NIRSpec integral field unit (IFU) studies at high redshifts to date have focused on UV-bright or massive objects, while our understanding of low-mass galaxies at early cosmic times remains limited. In this work, we present NIRSpec/IFU high-resolution observations of two low-mass ($M_* < 10^9$ $M_\odot$), low-metallicity ($[12 + \log(O/H)] < 8$) galaxies at $z \sim 7.66$, one of which we identify as hosting a Type-II active galactic nucleus (AGN). We measure flat strong-line metallicity gradients, suggestive of interstellar medium redistribution by outflows or past merging, but also identify tension with the direct-T_e metallicity gradient in one galaxy. We find the ionized gas phase in both galaxies to be dispersion-dominated, consistent with previous observations of lower rotational support at early cosmic times. We identify broad kinematical components decoupled from galactic rotation with velocities of $\sim 250 - 500$ km s^{-1} and argue these components trace outflows, for which we infer mass outflow rates of $\sim 8 - 14$ $M_\odot$ yr^{-1}. We compare our findings to results from the new large-volume AESOPICA simulations, which fully incorporate different models of black hole growth and AGN feedback. We find that our observationally measured ratios of outflow to escape velocity are consistent with those of the simulated dwarf AGN population, hinting that AGN-driven feedback may contribute to quenching in early low-mass galaxies such as our targets. This novel study illustrates the necessity of deep IFU observations to decompose the complex kinematics and morphology of high-z galaxies, trace outflows, and constrain the effects of feedback in the early Universe.

Key words: ISM: abundances – ISM: jets and outflows – galaxies: evolution – galaxies: high-redshift – galaxies: kinematics and dynamics.

1 INTRODUCTION

The launch of the *James Webb Space Telescope* (*JWST*), with its powerful near-infrared spectrograph (NIRSpec, T. Böker et al. 2022; P. Jakobsen et al. 2022), has enabled observations of rest-frame ultraviolet (UV) and optical emission above $z > 3$, and opened a new window for studying the physical properties of high-z galaxies (e.g. P. Arrabal Haro et al. 2023; E. Curtis-Lake et al. 2023; T. Y.-Y. Hsiao et al. 2023; M. Castellano et al. 2024; B. Robertson et al. 2024; S. Carniani et al. 2024a; R. Maiolino et al. 2024a; F. D'Eugenio et al. 2024b; C. T. Donnan et al. 2025; R.

★ E-mail: li247@cam.ac.uk

© The Author(s) 2026.
Published by Oxford University Press on behalf of Royal Astronomical Society. This is an Open Access article distributed under the terms of the Creative Commons Attribution License (https://creativecommons.org/licenses/by/4.0/), which permits unrestricted reuse, distribution, and reproduction in any medium, provided the original work is properly cited.

Downloaded from https://academic.oup.com/mnras/article/546/3/stag094/8426291 by guest on 31 March 2026

P. Naidu et al. 2025). These observations have shown that high-redshift galaxies have properties fundamentally different to those of local galaxies: lower metallicities (D. Schaerer et al. 2022; D. Langeroodi et al. 2023; K. Nakajima et al. 2023; M. Curti et al. 2024), high ionization parameters (A. J. Cameron et al. 2023; R. L. Sanders et al. 2023) and electron temperatures (M. Curti et al. 2023), increasing interstellar medium (ISM) densities (N. A. Reddy et al. 2023; Y. Isobe et al. 2023; C. Marconcini et al. 2024), and bursty star formation histories (SFHs; R. Endsley et al. 2023; A. Dressler et al. 2024; D. Langeroodi & J. Hjorth 2024; T. J. Looser et al. 2025; C. Witten et al. 2025c).

Observations with the *JWST* NIRSpec Integral Field Unit (IFU) have placed key constraints on spatially-resolved ISM properties, and traced the chemical enrichment of galaxies at high-z (S. Arribas et al. 2024; B. Rodríguez Del Pino et al. 2024; J. Scholtz et al. 2025c). For example, radial metallicity gradients, which bear the imprint of gas mixing by various galaxy evolutionary processes, have now been studied out to $z \sim 8$ (e.g. X. Wang et al. 2022; G. Venturi et al. 2024; R. Tripodi et al. 2024; S. Fujimoto et al. 2025; Z. Li et al. 2025), finding a significant diversity of negative, flat, and positive gradients. Such results are consistent with the diverse gradients measured by other studies up to Cosmic Noon (e.g. A. M. Swinbank et al. 2012; P. Troncoso et al. 2014; E. Wuyts et al. 2016; X. Wang et al. 2017; M. Curti et al. 2020b; R. C. Simons et al. 2021; A. Acharyya et al. 2025); these gradients encode the combination of inflows, outflows and mergers with underlying evolutionary processes and physical conditions in their host galaxies (L. J. Kewley, D. C. Nicholls & R. S. Sutherland 2019; R. Maiolino & F. Mannucci 2019), reflecting the diverse early galaxy population. However, results from simulations across a wide range of numerical methods and input physics suggest increasingly negative gradients at high redshift (e.g. Z. S. Hemler et al. 2021; A. M. Garcia et al. 2025b), in tension with observational results. As noted by A. M. Garcia et al. (2025a, b), there are currently no simulations which include how unresolved turbulence can redistribute mass and metals through throughout the galaxies, which may drive this tension. An comprehensive understanding of the underlying gas kinematics in high-z galaxies is therefore crucial to accurately modelling their chemical evolution and addressing the current tension between simulations and observations.

Spatially resolved spectroscopic surveys have demonstrated that many high-z galaxies have complex kinematics, including mergers or outflows (e.g. O. Le Fèvre et al. 2020; R. Herrera-Camus et al. 2025). Additionally, the observed velocity dispersion of disc-like galaxies appears to increase with redshift (e.g. E. Wisnioski et al. 2015; H. Übler et al. 2019; F. Rizzo et al. 2024; A. L. Danhaive et al. 2025), with the ionized gas phase typically showing higher dispersion than the cold/molecular gas phase (e.g. M. Girard et al. 2021). While some evidence for early dynamically cold discs has been found (F. Rizzo et al. 2020; F. Lelli et al. 2021; L. E. Rowland et al. 2024; J. Scholtz et al. 2025a), other NIRSpec/IFU observations have also revealed evidence of small-scale merging (e.g. C. Marconcini et al. 2024; G. C. Jones et al. 2025a; J. Scholtz et al. 2025c). Differences in sample selection, kinematical tracers, and spectral and angular resolution result in significant challenges to reliably comparing kinematics measured by existing studies. To build a full picture of galaxy kinematics in the early Universe, it is therefore crucial to complement existing studies of cold gas kinematics with those of warm, ionized gas, traced with *JWST* observations of [O III]λ5007 or Hα emission lines (e.g. A. Graaff et al. 2024; A. L. Danhaive et al. 2025).

Recent observations with *JWST* have found a large fraction of early low-mass ($M_* \lesssim 10^9\,M_\odot$) galaxies to exhibit bursty star formation (SF; R. Endsley et al. 2023; A. Dressler et al. 2024; T. J. Looser et al. 2025), while others are found to be 'mini-quenched' (or napping, e.g. V. Strait et al. 2023; T. J. Looser et al. 2024; C. Witten et al. 2025a; W. M. Baker et al. 2025b; A. Covelo-Paz et al. 2026). High-mass galaxies ($M_* \gtrsim 10^9\,M_\odot$) have also been found fully quenched at high redshift (A. C. Carnall et al. 2023b, c; K. Glazebrook et al. 2024; T. Nanayakkara et al. 2024, 2025; A. Weibel et al. 2025; C. Turner et al. 2025; W. M. Baker et al. 2025a, c). Theoretical models argue that massive, fully quenched galaxies cannot result from supernovae feedback alone; feedback driven by active galactic nuclei (AGNs) is likely necessary to explain their observed quenching (V. Gelli et al. 2024). Observations of quasar-host galaxies have indeed found results consistent with ionized outflows producing significant feedback even at $z > 4.5$ (E. Parlanti et al. 2024; M. Bischetti et al. 2024; A. Vayner et al. 2025; Y. Zhu et al. 2025). However, simulations are able to reproduce quenching in low-mass galaxies, with bursty SF found to be particularly important in the low-mass regime (T. Dome et al. 2024, 2025; S. Martin-Alvarez et al. 2026). Interestingly, *JWST* has unveiled an abundance of AGN at high redshift, both Type I (Y. Harikane et al. 2023; D. D. Kocevski et al. 2023; M. Onoue et al. 2023; H. Übler et al. 2023; L. J. Furtak et al. 2024; J. E. Greene et al. 2024; J. Matthee et al. 2024; R. Maiolino et al. 2024a, b; G. Mazzolari et al. 2024a; I. Juodžbalis et al. 2025; A. J. Taylor et al. 2025) and Type II (J. Brinchmann 2023; G. Mazzolari et al. 2025; S. Tacchella et al. 2025; J. Scholtz et al. 2025d), supporting claims that AGN feedback is already operating at early cosmic times. This raises an intriguing question: is AGN feedback contributing to the quenching of early low-mass galaxies?

Despite the abundance of AGN in the early Universe, finding evidence of AGN-driven feedback (e.g. outflows or hard ionizing radiation) remains difficult due to limited spectral and spatial resolution, as well as the complex morphologies of early galaxies (at $z > 7$; J. S. Kartaltepe et al. 2023; T. Treu et al. 2023), all of which limit our ability to accurately distinguish outflows from mergers, inflows or early discs. Efforts to investigate the presence of AGN- and SF-driven outflows in such high-z galaxies have been limited (S. Carniani et al. 2024b; Y. Xu et al. 2025), even though ionized gas outflows are known to be ubiquitous features of low-z AGN and high-luminosity quasi-stellar objects (QSOs; C. M. Harrison et al. 2016; M. Bischetti et al. 2017; D. Kakkad et al. 2020; G. Cresci et al. 2023; M. Perna et al. 2023; M. A. Marshall et al. 2025; M. Perna et al. 2025).

With *JWST*, it is now possible to explore ionized gas outflows, traced by Hα and [O III]λ5007 emission, in galaxies at high-z, even on spatially resolved scales. Indeed, numerous studies have found evidence for outflows, primarily by using NIRSpec in its integral field spectroscopy (IFS) mode, but also with its micro-shutter assembly (MSA) spectroscopy mode (e.g. M. A. Marshall et al. 2023; E. Parlanti et al. 2023; M. Perna et al. 2023; H. Übler et al. 2023, 2024; X. Ji et al. 2024; I. Lamperti et al. 2024; B. Rodríguez Del Pino et al. 2024; F. D'Eugenio et al. 2024a; G. C. Jones et al. 2024a; S. Carniani et al. 2024b; E. Bertola et al. 2025; P. G. Pérez-González et al. 2025; S. Zamora et al. 2025; J. Scholtz et al. 2025c). However, most of these studies focus on bright targets previously detected by HST and ALMA, resulting in an observational bias towards starburst galaxies or mergers (e.g. G. C. Jones et al. 2024a; E. Parlanti et al. 2025; J. Scholtz et al. 2025c). In fact, the new population of early intermediate- to low-luminosity AGN

Downloaded from https://academic.oup.com/mnras/article/546/3/stag094/8426291 by guest on 31 March 2026

found by *JWST* appears to show little evidence for AGN-driven feedback in their host galaxies (R. Maiolino et al. 2025b; J. Scholtz et al. 2025d; F. D'Eugenio et al. 2026). In particular, low-mass star-forming galaxies (SFGs) exhibit fewer outflows than expected, especially considering that *JWST* is probing the earliest phases of galaxy formation, when feedback processes were expected to be strongest according to some models (S. Carniani et al. 2024b; W. McClymont et al. 2025b). In contrast to these observations, one possibility that has emerged from recent simulations is that AGN feedback may play an important role in low-mass galaxies (S. Koudmani, N. A. Henden & D. Sijacki 2021; R. S. Sharma et al. 2023; E. Arjona-Gálvez, A. Di Cintio & R. J. J. Grand 2024), particularly in the early Universe, but that our observations are failing to detect this feedback. It could be that the observed deficit of outflows in low-mass galaxies may arise from MSA spectroscopy-based studies lacking the spatial resolution required to reliably decompose the complex kinematics of high-redshift galaxies and reliably identify outflow signatures. Deep, high-resolution IFS is certainly a more adequate tool to investigate the potential weak outflows in low-mass galaxies with low-luminosity AGN.

This study focuses on two galaxies observed by *JWST* as part of the Early Release Observations (PID: 2736, K. M. Pontoppidan et al. 2022), as presented in A. C. Carnall et al. (2023a) and J. R. Trump et al. (2023). Specifically, we discuss SMACS J0723.3−7327 NIRSpec-ID6355 and -ID10612 (henceforth ID6355 and ID10612, respectively), which belong to a spectroscopically confirmed protocluster at $z \sim 7.66$ (N. Laporte et al. 2022; C. Witten et al. 2025b). Both of these galaxies are weakly lensed (magnification $\mu \sim 1.2$; derived from the lens model of G. Mahler et al. 2023 by M. Curti et al. 2023), with stellar masses of $\log(M_*/\mathrm{M}_\odot) = 8.72 \pm 0.04$ and 8.08 ± 0.04 in ID6355 and ID10612, respectively (M. Curti et al. 2023), classifying them as low-mass galaxies, as the knee of the galaxy mass function is already 10^{10} $\mathrm{M}_\odot$ at $z \sim 6$ (A. Weibel et al. 2024). Both galaxies were followed up with NIRSpec/IFU observations as part of the GO 2959 programme (PI: Scholtz), obtaining the higher resolution $R2700$ spectra, which form the core of this work.

Furthermore, both galaxies discussed in this work are AGN-host candidates. Previous studies using the NIRSpec/MSA $R1000$ spectra of these targets have detected [Ne IV]λλ2422, 2424 emission in ID6355 (J. Brinchmann 2023; M. S. Silcock et al. 2025); this high ionization-energy emission line (~ 63 eV) is often associated with AGN activity (A. Feltre, S. Charlot & J. Gutkin 2016), and indicates that ID6355 hosts some source of ionization stronger than SF alone. While there was no direct detection of this line in ID10612, J. Brinchmann (2023) found by comparison that a majority of Sloan Digital Sky Survey (SDSS) galaxies with a [O III]λ4363/Hγ ratio within 1σ of that of ID10612 were classified as AGN based on the BPT diagnostic. This demonstrates there is a strong source of heating in ID10612, hinting at the presence of an AGN. We will further investigate this claim using our higher-resolution NIRSpec/IFU spectra and established AGN diagnostic diagrams.

Furthermore, by exploring the spatially resolved ISM properties and kinematics of our targets, we will investigate and characterize their outflows (if any). In doing so, we will take an important step towards quantifying the potential impact of AGN-driven feedback on the kinematics and evolution of early low-mass galaxies.

This paper is structured as follows: in Section 2, we describe the details of the observations and data reduction, then outline our analysis in Section 3. A characterization of galaxy properties, both integrated and spatially resolved, is presented in Section 4. Then, in Section 5, we analyse the kinematics of our targets. Our results will be discussed and situated within in a wider context in Section 6. Throughout this work, we assume a flat Lambda-cold dark matter model with $H_0 = 70$ km s^{-1} Mpc^{-3}, $\Omega_{m,0} = 0.3$, and $\Omega_{\Lambda,0} = 0.7$. We additionally take solar metallicity as $[12 + \log(\mathrm{O/H})]_\odot = 8.69$ (M. Asplund et al. 2009), and use the term low-metallicity to refer to $[12 + \log(\mathrm{O/H})] < 8$. Finally, we adopt the lensing factors $\mu = 1.23 \pm 0.01$ and 1.34 ± 0.01 for ID6355 and ID10612, respectively, as derived by M. Curti et al. (2023).

2 OBSERVATIONS AND DATA REDUCTION

2.1 NIRSpec data

Our target galaxies were observed with *JWST*/NIRSpec in IFS mode (T. Böker et al. 2022; P. Jakobsen et al. 2022). The NIRSpec data were taken on the 2024 May 29–30, with a medium cycling pattern of eight dither positions and a total integration time of 22.4 ks per galaxy (6.2 h on-source) with the high-resolution grating/filter pair $G395H/F290LP$, covering the wavelength range $2.87 - 5.27$ μm (spectral resolution $R \sim 2000 - 3500$; P. Jakobsen et al. 2022).

Raw data files of these observations were downloaded from the Barbara A. Mikulski Archive for Space Telescopes (MAST) and then processed with the *JWST* Science Calibration pipeline[1] version 1.15.0 under the Calibration Reference Data System (CRDS) context jwst_1293.pmap. We use the same modification of the pipeline as described in detail by M. Perna et al. (2023) in order to increase the data quality. We briefly summarize the steps here. Count-rate frames are corrected for $1/f$ noise through a polynomial fit based on an algorithm from M. Perna et al. (2023). Furthermore, we remove regions affected by failed-open MSA shutters during Stage 2 calibration, along with other artefacts such as snowballs. We also remove regions with strong cosmic ray residuals in several exposures. Any remaining outliers are flagged in individual exposures using an algorithm similar to LACOSMIC (P. G. Dokkum 2001): we calculate the derivative of the count-rate maps along the dispersion direction, normalize by the local flux [or by three times the root mean square (rms) noise; whichever is highest], and reject the 95th percentile of the resulting distribution (see F. D'Eugenio et al. 2024a, for details). The final cubes are combined using the 'drizzle' method. All analysis in this paper is based on the combined cube with a pixel scale of 0.05 arcsec.

We perform background subtraction of our data cubes by first extracting an integrated spectrum from all non-target spaxels, excluding spaxels containing noise spikes via visual inspection. This background spectrum is smoothed with a median filter of 25 pixels to reduce its remaining noise, then subtracted from the spectrum of each spaxel in our data cube. The estimated average background levels are $\sim 9 \times 10^{-20}$ and $\sim 6 \times 10^{-20}$ erg s^{-1} cm^{-2} Å^{-1} arcsec^{-2} in the ID6355 and ID10612 cubes, respectively.

2.2 Error extension correction

H. Übler et al. (2023) report that uncertainties on flux measurements in the ERR extension of the IFU data cubes are under-

[1] https://jwst-pipeline.readthedocs.io/en/stable/jwst/user_documentation/introduction.html

Downloaded from https://academic.oup.com/mnras/article/546/3/stag094/8426291 by guest on 31 March 2026

estimated compared to the noise estimated from the rms of the spectrum. However, the ERR extension still carries crucial information about outliers and the correlated noise between channels. Hence, whenever extracting a spectrum, we also retrieve the uncertainty from the ERR extension and scale it so that its median uncertainty matches the spectrum's σ-clipped rms in emission-line free regions on each detector. The scaling for each detector does not have a wavelength dependence. We utilize the corrected flux uncertainties to estimate sensitivities of $\sim 5 \times 10^{-21}$ and $\sim 3 \times 10^{-21}$ erg s^{-1} cm^{-2} Å^{-1} in the spectral region of Hβ and [O III]$\lambda\lambda$4959, 5007 for the ID6355 and ID10612 cubes, respectively.

2.3 NIRCam imaging

In this work, we also make use of NIRCam images from the original ERO programme of the SMACS J0723.3−7327 cluster (see Introduction); the data comprise imaging in six NIRCam bands (*F*090*W*, *F*150*W*, *F*200*W*, *F*277*W*, *F*356*W*, and *F*444*W*). A full description of the data reduction, including determination of the astrometry, is presented in S. Tacchella et al. (2023).

2.4 Astrometry realignment

As the field of view (FoV) of the NIRSpec/IFS observations is only 3×3 arcsec, we lack the multiple stars or point sources necessary to perform an accurate astrometry calibration. Therefore, we used NIRCam images (Section 2.3) to align the NIRSpec/IFS data to the correct astrometry, allowing us to reliably compare the location of the stellar continuum and emission lines. To do so, we first create a mock *F*444*W* image from the NIRSpec cube using the PYTHON package SEDPY (B. D. Johnson 2019). We identify the brightest pixel in the NIRCam *F*444*W* image, and match the WCS coordinates of the brightest mock-NIRCam spaxel to those of the *F*444*W* pixel. Later, when using the NIRSpec/IFU data cube for spaxel-by-spaxel fitting, the header of the cube is edited to capture this astrometric realignment.

We adopt an astrometry realignment based on the NIRCam *F*444*W* images for two key reasons. First, this filter contains the [O III]λ5007 emission that is the main focus of our kinematical study, and so this method guarantees alignment between the location of the peak [O III]λ5007 flux in the NIRSpec and NIRCam data. Secondly, both galaxies appear bright in this filter with good signal-to-noise ratios (SNR). Although the *F*356*W* filter has a smaller point spread function (PSF) and could, in theory, yield a more accurate realignment, our goal is to guarantee the best alignment for [O III]λ5007 emission specifically, so the limitation lies with the IFU data rather than NIRCam.

As all NIRCam filters are aligned with respect to each other, only a single astrometric realignment is required for each galaxy. We additionally check the astrometry corrections based on the *F*356*W* filter, as well as those based on a single star in the FoV of ID6355 observations (see Appendix A). All methods yield consistent astrometric realignments within the errors.

3 DATA ANALYSIS

3.1 Emission-line fitting

To determine the emission-line properties of our sources, we first extract their integrated spectra from a circular aperture ($r \sim 0.25$ arcsec), centred on the [O III]λ5007-brightest spaxel in each galaxy. This aperture is chosen as it is sufficiently large to avoid aperture loss from PSF sampling without reducing the SNR of emission lines in the spectrum. We then fit these integrated spectra using a least-squares fitting code, modelling the emission lines as a series of Gaussian profiles. We fit the following emission lines: Hβ, Hγ, Hδ, [O III]$\lambda\lambda$4959, 5007, [O III]λ4363, [O II]$\lambda\lambda$3727, 29, and [Ne III]$\lambda\lambda$3869, 3968. As He II $\lambda\lambda$4686 falls right on the edge of the detector gap in the spectra of both galaxies, it has not been included in either full spectral fit. We additionally include a linear component to model the continuum, which is too weak in either galaxy to be reliably fit with a stellar continuum, and which may contain some residual background. As our analysis focuses on the emission lines, modelling the continuum in this way does not impact our results.

Our primary ('narrow-line') model consists of a single Gaussian per emission line; the redshift and intrinsic full width half-maximum (FWHM) of each Gaussian profile are tied together to reduce the number of free parameters, but the flux of each is left free unless a specific line ratio is applied due to underlying atomic physics. The [O III]$\lambda\lambda$4959, 5007 flux ratio is fixed to 2.99 (M. S. Dimitrijević et al. 2007) and the [Ne III]$\lambda\lambda$3869, 3968 flux ratio is fixed to 3.32 (e.g. G. C. Jones et al. 2024a), while the [O II]$\lambda\lambda$3727, 29 flux ratio is allowed to vary to reflect its dependence on electron density (R. L. Sanders et al. 2015). For each emission line, the FWHM is convolved with the NIRSpec line spread function, as retrieved from the JDox.[2]

We also fit each spectrum with a 'two-Gaussian model', which is identical to the primary model but additionally includes a broad Gaussian profile in Hβ and [O III]$\lambda\lambda$4959, 5007. This model includes an FWHM threshold at 200 km s^{-1} as an upper limit on the narrow component, ensuring that the fitted broad component is always broader than the fitted narrow component. Similarly to the primary model, the broad components of the Hβ and [O III]$\lambda\lambda$4959, 5007 lines have the redshift and FWHM of their Gaussian profiles tied together, but the broad parameters vary independently from the narrow ones. Hβ and [O III]$\lambda\lambda$4959, 5007 are the only lines in our spectra with sufficient SNR to enable detection of a broad component in the line profile. The minimum SNR threshold considered for the [O III]λ5007 emission line in a fit is 3. We show the galaxy-integrated spectra and their best fits, with both models, in Fig. 1.

We repeat the spectral fitting, now spaxel by spaxel, in the region covered by each target, using the same models and overall method as described above. When fitting each spaxel, we first average its spectrum and combine its errors with those of the eight surrounding spaxels (i.e. within a radius of 0.07 arcsec). As the spaxel size oversamples the PSF of our observations, this increases the SNR of the detected emission lines without reducing the spatial resolution.

Whether the fit to a given spaxel accepts a broad component is statistically determined through two criteria: first, when comparing the Bayesian information criterion (BIC) of the narrow-line and two-Gaussian models we require $\Delta\mathrm{BIC} < -10$ (i.e. $\Delta\mathrm{BIC} = \mathrm{BIC}_{2-\mathrm{Gaussian}} - \mathrm{BIC}_{\mathrm{narrow}}$); and secondly, the broad component must have velocity-integrated SNR > 5. Both criteria must be satisfied to favour the two-Gaussian model. This procedure prevents overfitting of the data by only allowing an additional broad component to be fit if its inclusion is statistically favoured. The

[2]Available here.

Downloaded from https://academic.oup.com/mnras/article/546/3/stag094/8426291 by guest on 31 March 2026

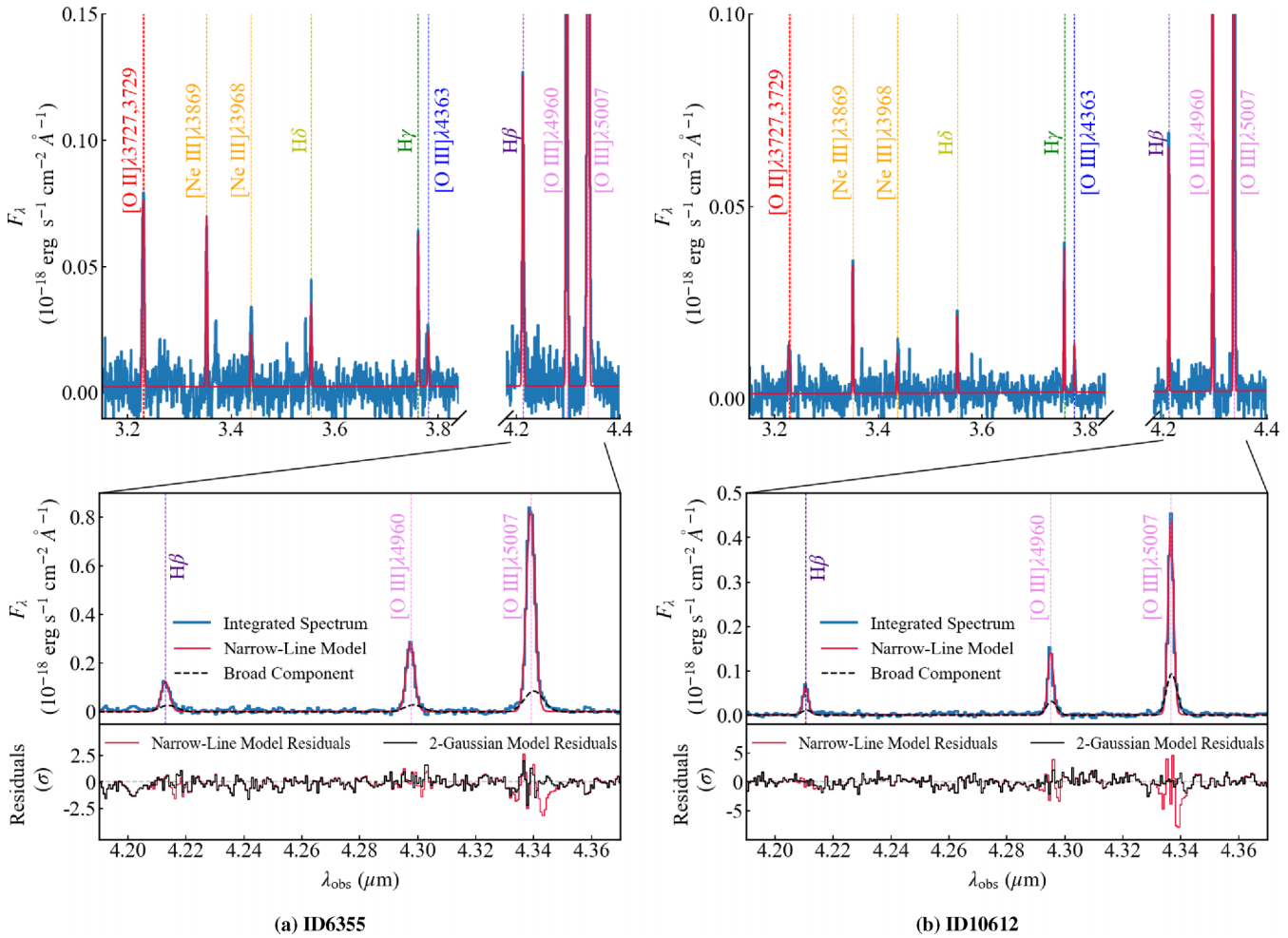

Figure 1. Summary of background-subtracted integrated spectra, fitted models, and model residual comparisons in both target galaxies. Top panels: full *R*2700 integrated spectra from the NIRSpec/IFU observations, extracted from circular apertures of radius 5 pixels (0.25 arcsec), centred on the [O III]λ5007 brightest spaxel in each galaxy. The background-subtracted integrated spectrum is plotted in blue, and the fitted narrow-line model (see Section 3.1) in red. The axes have been cut to eliminate the detector gap in each spectrum from the plots. The spectra shown here have not been continuum-subtracted, as the spectral fitting accounts for the weak continuum with a linear continuum model. Middle panels: a zoom-in on the Hβ and [O III]λλ4959, 5007 emission lines, showing how these lines are now fitted with the two-Gaussian model. (a)Shows the fitted broad component in ID6355 is clearly offset from the narrow-line component, suggesting the presence of non-rotational kinematics such as an outflow or merger. The small feature visible blueward of Hβ in the spectrum of ID6355 is a noise feature close to the detector gap, and our analysis based on SNR and BIC also shows that this feature does not meet our criteria for a detected emission-line wing. (b) Shows the offset between the broad and narrow components is less distinct in ID10612. Bottom panels: a comparison of narrow-line and two-Gaussian model χ residuals, illustrating the necessity of including broad components for Hβ and [O III]λλ4959, 5007 in our fit.

spaxels with evidence for a broad component hence robustly map the spatial extent of this component. For simplicity, the region of spaxels in each galaxy fitting with an additional broad component will henceforth be referred to the 'outflow region' of that galaxy. We further discuss the origin of this broad component in Section 5.4.

We present flux maps of the fitted forbidden and Balmer emission lines in Figs 2 and 3, and note that the narrow and broad components of [O III]λ5007 integrated flux are mapped in panels (i) and (ii) of Figs 7(a) and (b) later in the paper. [O III]λ5007 and Hβ are the brightest detections in both galaxies, with all other emission lines about an order of magnitude fainter. The centroid of each emission line approximately coincides with the centroid of [O III]λ5007 emission as indicated in Figs 2 and 3, though Hβ emission in particular appears to be extended away from this centroid in both galaxies.

Our resolved detections of [O III]λ4363 emission in each galaxy are particularly important, as [O III]λ4363 is a key emission line in AGN diagnostics effective at high-redshift (see Section 4.1). The extended ($r > 0.1$ arcsec), spatially resolved detections of the emission lines shown in Figs 2 and 3 also allow us to investigate the metallicity profiles of our targets (see Section 4.3). From the results of our spaxel-by-spaxel fitting, we will also present the [O III]λ5007-derived kinematics maps of our targets later on in Section 5.1.

3.2 Dust corrections and gas metallicity calibration

Before estimating metallicity, it is important to first take into account any dust reddening affecting the emission lines. We use the available Balmer emission lines to perform this correction, in particular the Hγ/Hβ ratio, when both lines are detected with SNR

Downloaded from https://academic.oup.com/mnras/article/546/3/stag094/8426291 by guest on 31 March 2026

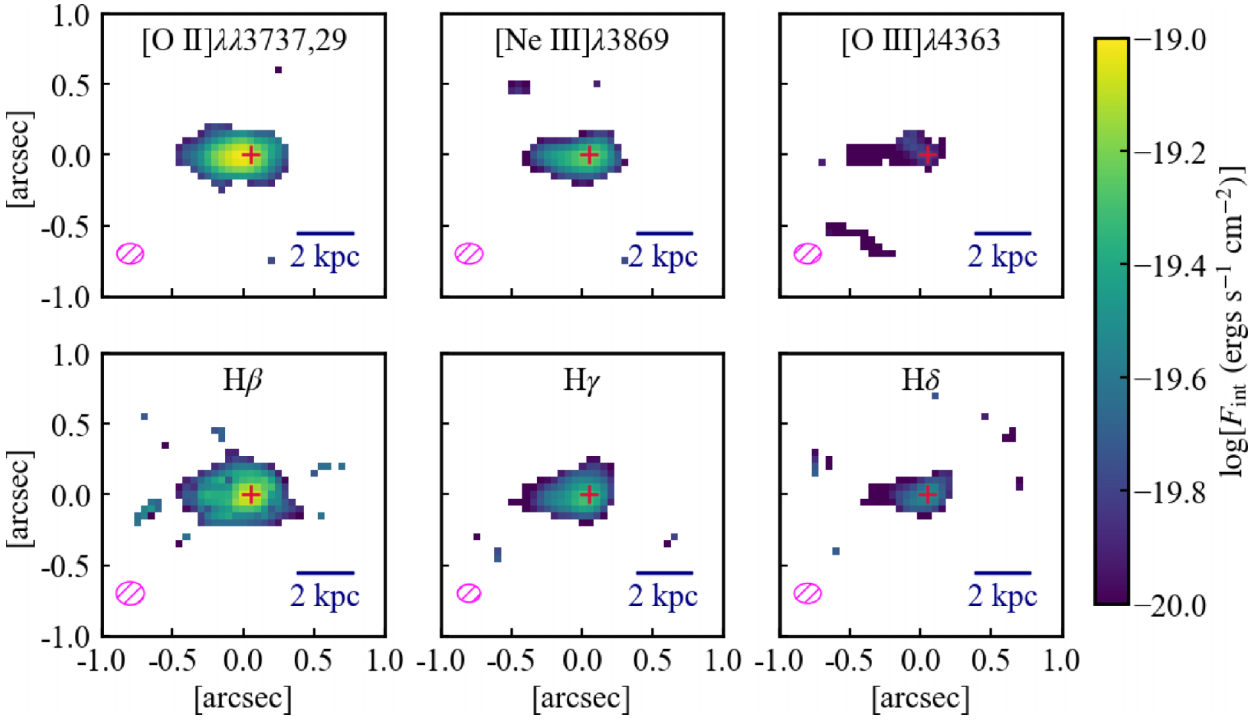

Figure 2. Resolved (SNR > 3) emission-line maps of ID6355. Integrated fluxes, measured per spaxel, are plotted in log space to illustrate the relative brightness of each line. The magenta hatched ellipse in the bottom left of each plot illustrates the *JWST*/NIRSpec PSF of the relevant emission line. The red cross on each figure corresponds to the centroid of [O III]λ5007 integrated flux. Fluxes are uncorrected for dust attenuation. Top row: detected forbidden lines, from left to right: [O II]λλ3727, 29, [Ne III]λ3869 , and [O III]λ4363. Bottom row: detected Balmer lines, from left to right: Hβ, Hγ, and Hδ.

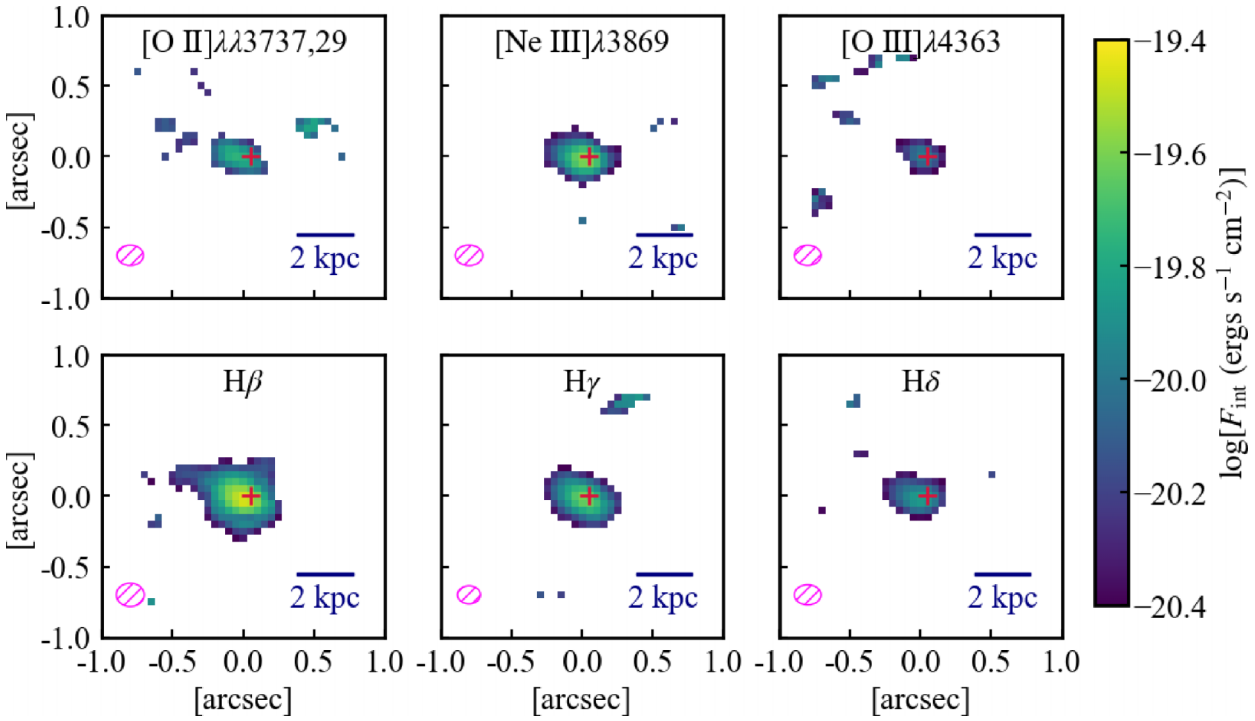

Figure 3. Resolved (SNR > 3) emission-line maps of ID10612. Integrated fluxes, measured per spaxel, are plotted in log space to illustrate the relative brightness of each line. The magenta hatched ellipse in the bottom left of each plot illustrates the *JWST*/NIRSpec PSF of the relevant emission line. The red cross on each figure corresponds to the centroid of [O III]λ5007 integrated flux. Fluxes are uncorrected for dust attenuation. Top row: detected forbidden lines, from left to right: [O II]λλ3727, 29, [Ne III]λ3869 , and [O III]λ4363. Bottom row: detected Balmer lines, from left to right: Hβ, Hγ, and Hδ.

Downloaded from https://academic.oup.com/mnras/article/546/3/stag094/8426291 by guest on 31 March 2026

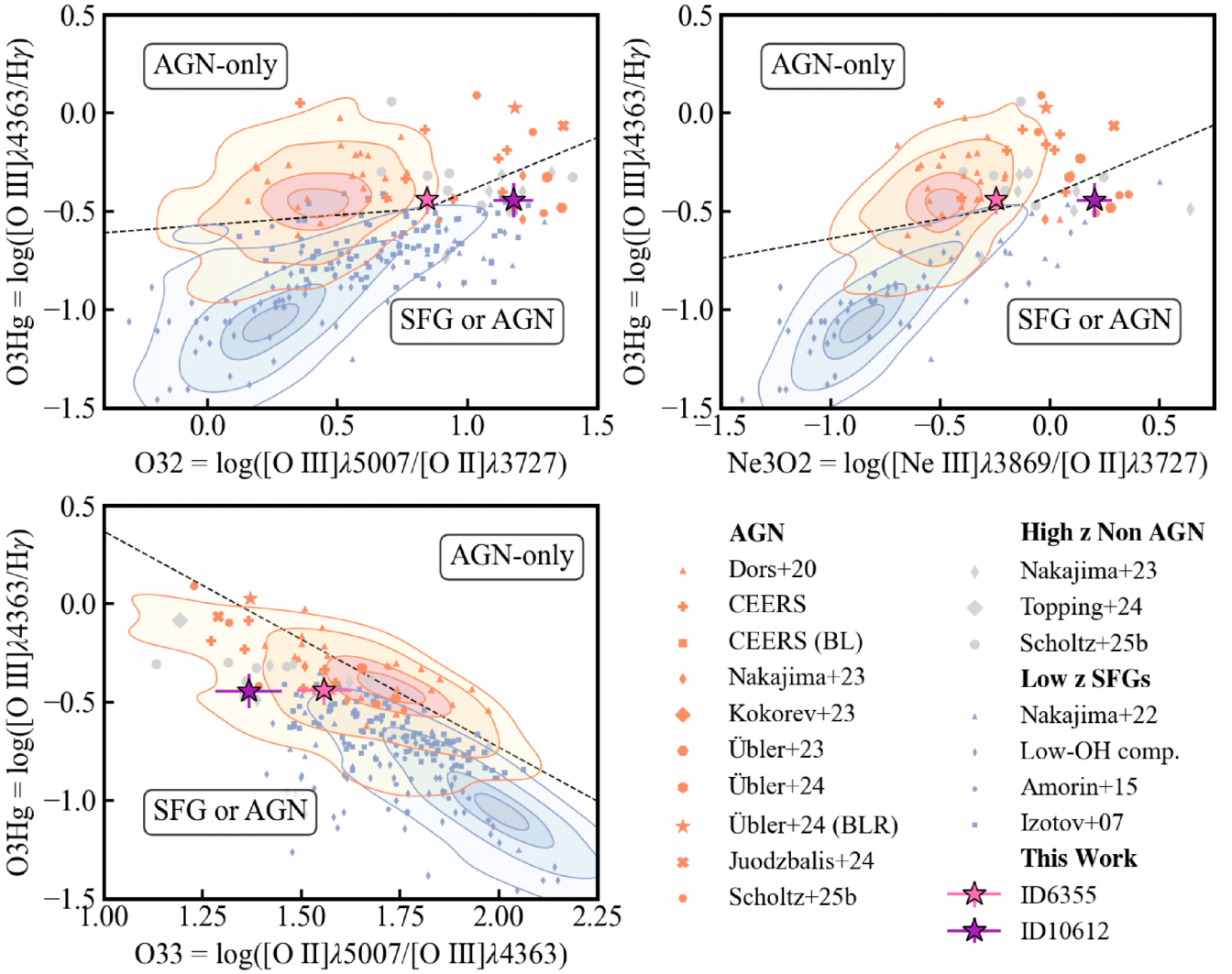

Figure 4. [O III]λ4363-based AGN diagnostic diagrams (G. Mazzolari et al. 2024b). ID6355 and ID10612 are plotted as the pink and purple stars, respectively. Orange points correspond to high-z AGN, blue points to low-z SFGs, and grey points to high-z sources not classified as AGN; the sample shown in these plots is compiled from Y. I. Izotov & T. X. Thuan (2007); R. Amorín et al. (2015); O. L. Dors et al. (2020); K. Nakajima et al. (2022); V. Kokorev et al. (2023); K. Nakajima et al. (2023); H. Übler et al. (2023, 2024); I. Juodžbalis et al. (2024); M. W. Topping et al. (2024); and J. Scholtz et al. (2025c). The low-OH compilation comprises sources from Y. I. Izotov et al. (2006, 2018, 2019); D. A. Berg et al. (2012), and S. A. Pustilnik et al. (2020, 2021). Orange and blue contours show the distribution of SDSS AGN and SFGs, respectively, including the 90 per cent, 70 per cent, 30 per cent, and 10 per cent of the populations. Demarcation lines between AGN-only and SFR/AGN regions are plotted as dashed black lines. Fluxes were not corrected for dust attenuation.

> 3. We assume the theoretical extinction-free Hγ/Hβ intrinsic ratio of 0.466, valid for case-B recombination and an electron temperature of $T_e \sim 10^4$ K (D. E. Osterbrock & G. J. Ferland 2006), typical of warm ionized gas emitting rest-frame optical lines such as [O III]λ5007 (and consistent with T_e measured for these galaxies by M. Curti et al. 2023). To evaluate the dust attenuation A_V, we adopt a method similar to the Balmer decrement approach (e.g. D. Calzetti, A. L. Kinney & T. Storchi-Bergmann 1994; A. Domínguez et al. 2013), replacing the Hα/Hβ relations with those applicable for Hγ/Hβ:

$$A_V = -2.5 \log_{10} \left(\frac{F_{H\gamma}/F_{H\beta}}{0.466} \right) \frac{R_V}{k_{H\gamma} - k_{H\beta}}, \quad (1)$$

where $R_V = 4.05$, and $k_{H\gamma}$ and $k_{H\beta}$ correspond to the relevant dust attenuation curve evaluated at the rest-frame wavelengths of Hγ and Hβ, respectively. In this work, we apply the dust attenuation curve presented in D. Calzetti et al. (2000), with $R_V = 4.05$, which is suitable for high-z, low-metallicity galaxies at the wavelengths of interest here (I. Shivaei et al. 2020), and similar to the approach adopted in G. Venturi et al. (2024).

We note that the Balmer line ratio may also be affected by stellar absorption (B. Groves, J. Brinchmann & C. J. Walcher 2012), and it is possible to account for this through knowledge of stellar populations obtained from spectral energy distribution (SED) fitting (e.g. as done by S. Tacchella et al. 2023). However, the difference in spectral resolution between the MSA and IFU observations makes accurate spectral comparison difficult, so we neglect potential stellar absorption effects for the purposes of this work.

In the case of an integrated spectrum, dust correction is based on the integrated Hγ/Hβ ratio, as the aperture is sufficiently large to render PSF effects negligible. In the case of spaxel-by-spaxel

Downloaded from https://academic.oup.com/mnras/article/546/3/stag094/8426291 by guest on 31 March 2026

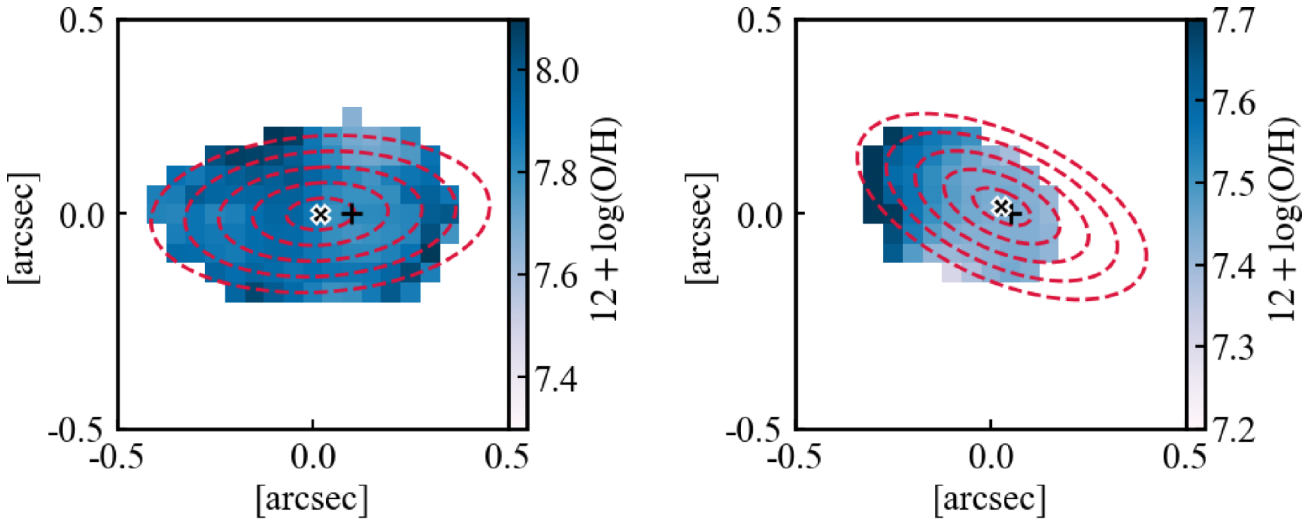

(a) ID6355 **(b) ID10612**

Figure 5. Strong-line metallicity maps of each galaxy calculated from [O III]λ5007 PSF-matched cubes, using calibrations from E. Cataldi et al. (2025) and the line ratios from Table 1, in spaxels where SNR> 3 for all relevant emission lines. The [O III]λ5007 flux centroid of each galaxy is indicated by a black cross on the relevant plot. The morphological centre obtained from PySersic fitting (see Section 3.3) is shown as the white-outlined cross on each plot. The annular regions from which the metallicity gradients are derived (Fig. 6) are highlighted by the red dashed circles on each plot. The average error in metallicity for an individual spaxel is ∼ 0.25 dex for ID6355 and ∼ 0.16 dex for ID10612; hence, both maps are consistent with flat metallicity profiles.

measurements, we first PSF match our data cubes to the worst PSF, i.e. the PSF at the wavelength of [O III]λ5007. This is done to mitigate the effects of PSF variation across different wavelengths on spatially resolved metallicity measurements. We then apply dust corrections to spectra extracted from the PSF-matched cube according to their measured Hγ/Hβ ratios. After dust correction, we estimate metallicity from the corrected fluxes using two separate methods: strong-line calibrations (e.g. M. Curti et al. 2020a; E. Cataldi et al. 2025; see Table 1) and the so-called direct-T_e method.

We use updated strong-line calibrations, as presented by E. Cataldi et al. (2025) for $z \sim 2-3$, to explore the spatial metallicity variation across each galaxy. While these calibrations are based on observations at lower redshifts than our objects, they are still more appropriate to study $z \sim 7.6$ galaxies than calibrations based on local-Universe measurements (e.g. M. Curti et al. 2020a). In general, we find assuming different metallicity calibrations (e.g. see R. Maiolino & F. Mannucci 2019 for extensive discussion; M. Curti et al. 2020a; K. Nakajima & R. Maiolino 2022; R. L. Sanders et al. 2023; I. H. Laseter et al. 2024) can introduce systematic uncertainties of $\gtrsim 0.2$ dex. Furthermore, all strong-line calibrations are based on radiation fields typical of star-forming regions; if AGN are present, line ratios can deviate significantly from the SF calibrations due to the hardness of AGN radiation. This can result in inaccurate measurements of overall metallicities and false metallicity gradients. As strong-line measurements are highly uncertain, especially at high redshift, we utilize all five of the strong-line calibrations shown in Table 1 to obtain the best possible constraint on strong-line metallicity.

For the direct-T_e method, we derive the temperature of the [O III]-emitting gas (O^{++}) by exploiting the high SNR detection of [O III]λ5007 and [O III]λ4363 in the *R*2700 spectra. We simultaneously derive gas density using the [O II]λλ3727, 3729 doublet ratio, whose lines are detected with SNR>3 in the *R*2700 integrated spectrum of ID6355. The temperature of the O^+ emitting region (hereafter t_2) is assumed to follow the temperature-temperature relation from Y. I. Izotov et al. (2006), i.e. $t_2 = 0.693t_3 + 2810$, where t_3 is the temperature of the O^{++} emitting gas.

With the derived temperature and density of the O^{++} gas, we then estimate the relative ionic abundances of oxygen and hydrogen using the intensity of each species, taking into account the different temperature- and density-dependent volumetric emissivity of the transitions using PyNeb (V. Luridiana, C. Morisset & R. A. Shaw 2015). With this method, we derive the O^{++}/H and O^+/H ratios from the [O III]λλ4959, 5007/Hβ (assuming t=t_3) and [O III]/Hβ (assuming t=t_2) ratios, respectively, and compute the total oxygen abundance as $O/H = O^+/H + O^{++}/H$. The direct-T_e metallicity is then computed as $[12 + \log(O/H)]$.

Using the integrated and spatially resolved emission-line properties, we estimate the metallicity properties of our galaxies on both integrated (Section 4.2.3) and spatially resolved (Section 4.3) scales. Our main approach to studying spatially resolved metallicity is to fit spectra extracted from concentric elliptical annuli and obtain radial gradients. We also map strong-line metallicity on a spaxel-by-spaxel basis using the [O III]λ5007 PSF-matched cubes.

On a spaxel-by-spaxel basis, it is not always possible to correct a given spaxel for dust extinction, as Hγ is not as extended as Hβ in either galaxy (see Figs 2 and 3). However, we only require spatially resolved dust correction for our metallicity analysis. In the case of metallicity gradients, these are derived from spectra integrated across multiple spaxels so each line is detected with sufficient SNR to enable correction. For the strong-line metallicity maps, the metallicity associated to a given spaxel is only calculated when both Hβ and Hγ are detected with SNR> 3 in its spectrum.

Downloaded from https://academic.oup.com/mnras/article/546/3/stag094/8426291 by guest on 31 March 2026

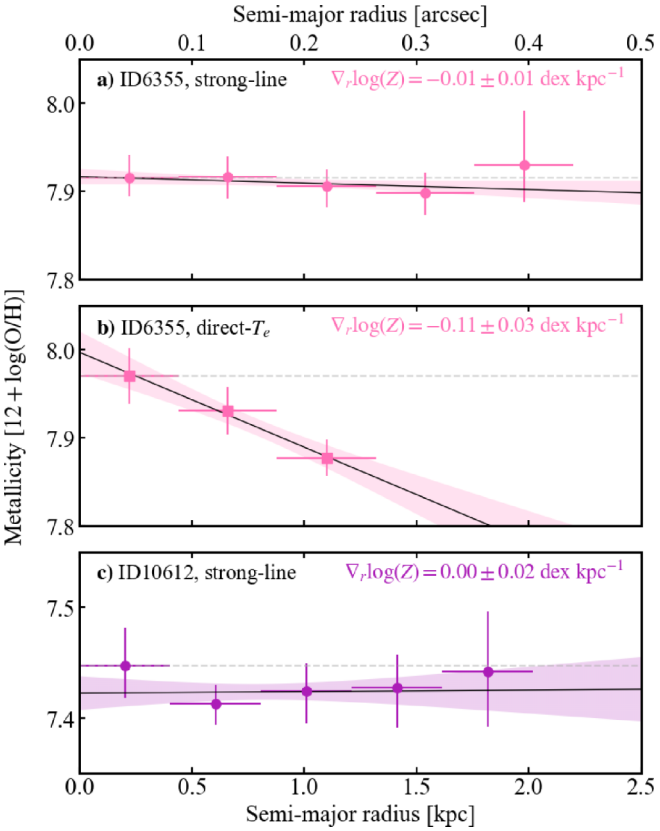

Figure 6. Metallicity gradients for our targets, determined from binned spectra extracted from the elliptical apertures shown in Fig. 5. Top two panels: (a) strong-line and (b) direct-T_e gradients in ID6355. Bottom panel, (c): strong-line metallicity gradient for ID10612. Fluxes are corrected for dust attenuation (Section 3.2), and strong-line metallicity is calculated using the E. Cataldi et al. (2025) calibrations with all five diagnostic ratios shown in Table 1, where SNR > 3 for the relevant emission lines. The horizontal grey dashed line on each plot illustrates the corresponding central metallicity value, while the solid black line indicates the best-fitting linear profile. The shaded region shows the uncertainty associated to the best fit. The calculated metallicity gradient, along with errors quoted at the 68 per cent confidence level, are quoted together on each plot.

3.3 Estimating morphological parameters

To obtain the morphological parameters of each source, we fit the NIRCam *F*444*W* filter images (see Section 2.3) with a one-component Sérsic model using the Bayesian code PySersic (I. Pasha & T. B. Miller 2023). The fitted parameters include ellipticity (e), Sérsic index (n), effective radius (R_e), and position angle (θ). From these parameters, we then estimate further physical properties of the galaxies, including their inclination (i). While performing the morphological fitting assumes the galaxy has a Sérsic brightness profile, no assumptions were made about the location of the photometric or kinematic centre of the galaxy.

The fitted and derived galaxy properties are summarized together in Table 2; the models, residuals and posterior corner plots produced from our PySersic fit are presented in Appendix C. The fitted morphological centres are illustrated in Fig. 5 later in the paper, and we find the fitted morphological centres are slightly offset from the [O III]λ5007 flux centroids. Interestingly, we identify half-light radii $R_e > 1$ kpc in both galaxies, which are unexpectedly large for low-mass galaxies at such high redshifts (T. Morishita et al. 2024; L. Westcott et al. 2025; N. Allen et al. 2025; T. B. Miller et al. 2025; W. McClymont et al. 2025c).

The axis ratio $q = b/a$ (ratio of scale height to scale length) is related to the ellipticity by

$$q = 1 - e. \tag{2}$$

Galaxy discs are widely thought to be thicker at high redshifts (A. der Wel et al. 2014), so the inclination i of the disc is calculated from the measured axis ratio q, as demonstrated in R. B. Tully et al. (1998):

$$\cos i = \left(\frac{q^2 - q_0^2}{1 - q_0^2} \right)^{1/2}, \tag{3}$$

where q_0 is the intrinsic axial ratio of a perfectly edge-on disc galaxy; typically $q_0 \sim 0.2$ for a thin disc. We note that the choice of q_0 within its typical range, $0.0 - 0.2$, does not strongly impact inferred kinematical properties (S. H. Price et al. 2020; N. M. Förster Schreiber & S. Wuyts 2020).

4 GALAXY PROPERTIES

4.1 Auroral line AGN diagnostics

Previous works (J. Brinchmann 2023; M. S. Silcock et al. 2025) have concluded there is evidence to support the presence of AGN in our target galaxies. Here, we further investigate this claim by utilizing [O III]λ4363 auroral line-based diagnostics from G. Mazzolari et al. (2024b), which have been shown to reliably identify AGN at high redshift (I. Juodžbalis et al. 2025; G. Mazzolari et al. 2025).

We present the [O III]λ4363 diagnostics in Fig. 4, where it can be seen that ID6355 nominally falls in the AGN-only region in two out of three diagrams. Although the points cross the demarcation lines within their uncertainties, given the additional evidence of a high-ionization source from the detected [Ne IV] emission in this galaxy (J. Brinchmann 2023; M. S. Silcock et al. 2025), the diagnostics are consistent with the interpretation of ID6355 as hosting an AGN. Furthermore, as the Hβ emission line does not show evidence for broadening outside of the broad component also associated with the [O III]λλ4959, 5007 emission, this suggests ID6355 hosts a Type-II (narrow-line) AGN.

On the other hand, the line ratios of ID10612 are consistent with either SF or AGN activity across all three diagrams; therefore, we still lack conclusive evidence for an AGN being the dominant source of ionization in this galaxy. However, we note that G. Mazzolari et al. (2024b) have emphasized that their demarcation lines are very conservative, and that the AGN-only region likely extends by 0.25–0.5 dex below the lines they provide (see further discussion in G. C. Jones et al. 2025b).

To estimate an upper limit on bolometric luminosity, we utilize the dust-corrected narrow-line Hβ fluxes from the galaxy-integrated spectra. With the calibrations reported in H. Netzer (2009), we estimate $\log_{10}(L_{\rm bol}/{\rm erg\ s^{-1}}) \sim 45.7 - 46.2$ in our targets. However, these calibrations assume the lines used to derive $L_{\rm bol}$ are dominated by the AGN emission. This assumption is not necessarily true as we are considering the galaxy-integrated spectra, and therefore the estimated $L_{\rm bol}$ represent upper limits. Furthermore, depending on the calibration adopted (e.g. A. Lamastra et al. 2009, Hirschmann et al., in preparation), uncertainties in the estimated $L_{\rm bol}$ can go up to ∼ 1 dex.

Downloaded from https://academic.oup.com/mnras/article/546/3/stag094/8426291 by guest on 31 March 2026

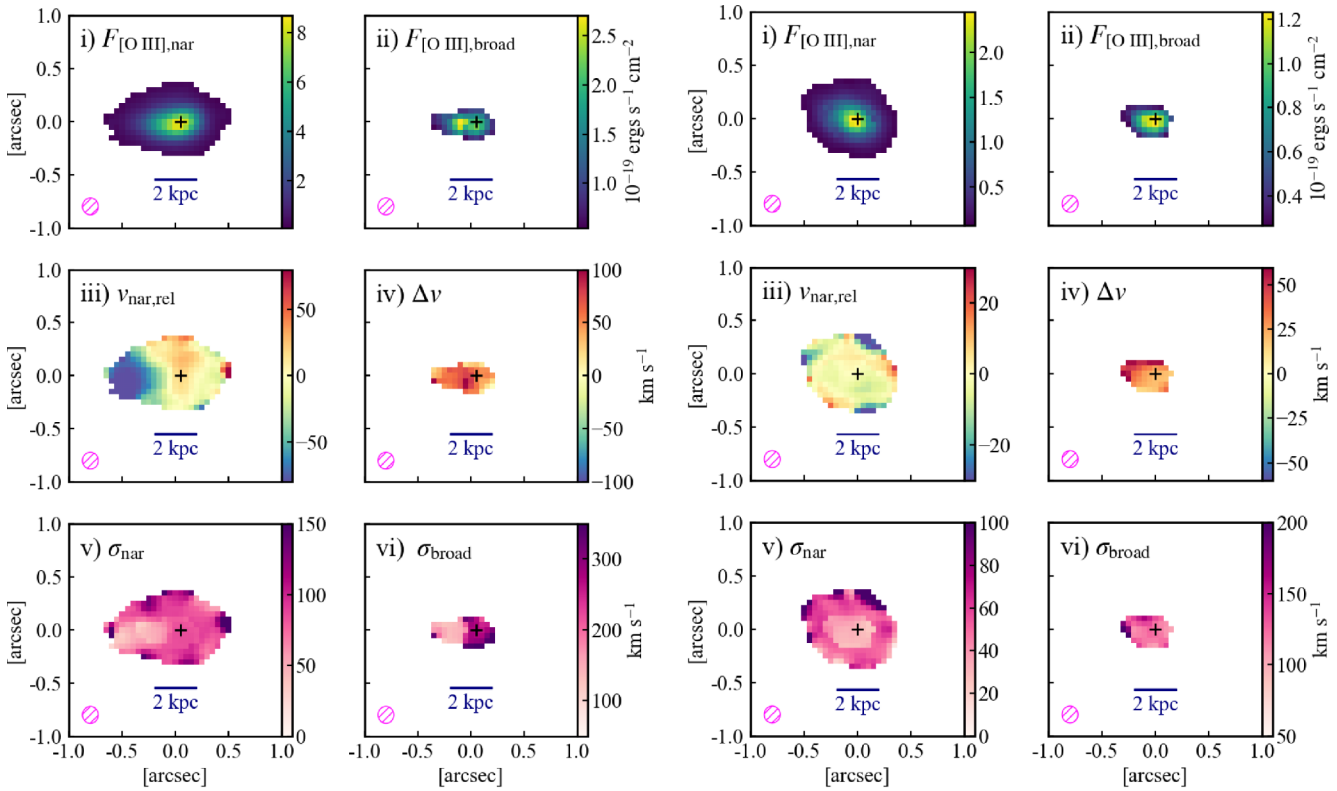

Figure 7. [O III]λ5007 kinematic maps of each galaxy, comparing the narrow (left column) and broad (right column) components in each galaxy. These are plotted for all spaxels with [O III]λ5007 SNR>5 for the respective component. The magenta hatched ellipse in the bottom left of each plot indicates the size of the NIRSpec/IFS PSF at the wavelength of the [O III]λ5007 emission line, and a 2 kpc scale bar is also included. The black cross on each figure corresponds to the centroid of [O III]λ5007 integrated flux. Individual panels in each figure show the following maps: (i) narrow component of [O III]λ5007 integrated flux; (ii) broad component of [O III]λ5007 integrated flux; (iii) $v_{nar,rel}$, the narrow-line velocity relative to the systematic galaxy velocity; (iv) Δv, the velocity offset between the narrow and broad components; (v) σ_{nar}, the intrinsic velocity dispersion of the narrow component; and (vi) σ_{broad}, the intrinsic velocity dispersion of the broad component.

Table 1. Emission-line diagnostic ratios used in this work, together with their compact notation. For further discussion of these calibrations, see e.g. M. Curti et al. (2020a).

Name	Emission-line ratio
R_2	[O II]λλ3727, 3729/Hβ
R_3	[O III]λ5007/Hβ
$\hat{R}$	0.47 R_2 + 0.88 R_3
O_3O_2	[O III]λ5007/[O II]λλ3727, 3729
Ne_3O_2	[Ne III]λ3869/[O II]λλ3727, 3729

4.2 Integrated galaxy properties

We report the galaxy-integrated best-fitting parameters of the narrow and broad components of a two-Gaussian model fit to each galaxy (see Section 3.1) in the upper segment of Table 3. Importantly, we note that uncertainties in the derived quantities are dominated by systematic uncertainties from the calibrations used in our analysis, rather than from the random flux uncertainties in our measurement. As our quoted uncertainties on the final derived values are determined from the random uncertainties, they should be considered as a lower limit on the true error. In Table 3, we additionally present some derived galaxy properties, as described across the following subsections.

Table 2. Summary of galaxy parameters obtained by fitting NIRCam *F444W* images of our targets with PySERSIC. Top segment: parameters obtained directly from the PySersic fits. Bottom segment: derived galaxy parameters. The axis ratio and inclination are calculated from the fitted ellipticity; see Equations (2) and (3). Errors are quoted at the 68 per cent confidence level and are derived from the PySersic fitting posteriors. The uncertainties quoted here exclude systematic errors not accounted for by the modelling and should therefore be taken as a lower limit.

Parameter	Unit	Value	
		ID6355	ID10612
e		0.54 ± 0.01	0.53 ± 0.01
n		0.95 ± 0.03	$2.63^{+0.13}_{-0.14}$
R_e	pixel	$5.75^{+0.05}_{-0.04}$	$6.45^{+0.19}_{-0.18}$
R_e	kpc	1.45 ± 0.01	1.63 ± 0.05
θ	°	93.4 ± 0.6	65.3 ± 1.1
q		0.46 ± 0.01	0.47 ± 0.01
i	°	65.0 ± 0.7	64.3 ± 0.7

4.2.1 *Dust attenuation*

Table 3 shows the observed ratio of integrated Hγ/Hβ fluxes ($F_{H\gamma}/F_{H\beta}$) calculated from our spectral fitting, from which we also calculate the attenuation A_V and its associated error (see Section 3.2). We estimate A_V in ID6355 as $0.3^{+0.6}_{-0.3}$, indicative of low dust

Downloaded from https://academic.oup.com/mnras/article/546/3/stag094/8426291 by guest on 31 March 2026

Table 3. Summary of galaxy properties, derived from integrated spectra extracted from the apertures described in Section 3.1, with the exception of SFR, which is determined from an integrated spectrum extracted from a circular aperture of radius 0.5 arcsec (ID6355) or 0.4 arcsec (ID10612). Errors were bootstrapped from the spectral fitting uncertainties and are quoted at the 68 per cent confidence interval. We note that errors will always be dominated by systematics, including systematic uncertainties on the flux calibration of the instrument ($\sim$ 10 per cent, J. Scholtz et al. 2025b), so the errors quoted here and throughout the rest of this work represent a statistical lower bound on the true error. Quoted fluxes have been corrected for dust correction where possible.

		ID6355	ID10612
Redshift		7.66360 ± 0.00003	7.65883 ± 0.00002
$\mathrm{FWHM_{narrow}}$	km s^{-1}	189 ± 4	70 ± 4
$\mathrm{FWHM_{broad}}$	km s^{-1}	522 ± 47	275 ± 12
Δv	km s^{-1}	79 ± 21	25 ± 4
$F_{\mathrm{[O\ III]}\lambda5007,\mathrm{narrow}}$	10^{-18} erg s^{-1} cm^{-2}	25.6 ± 0.8	6.8 ± 0.3
$F_{\mathrm{[O\ III]}\lambda5007,\mathrm{broad}}$	10^{-18} erg s^{-1} cm^{-2}	7.1 ± 1.5	4.2 ± 0.4
$F_{\mathrm{H}\beta}$	10^{-18} erg s^{-1} cm^{-2}	4.4 ± 0.2	1.5 ± 0.1
$F_{\mathrm{H}\gamma}$	10^{-18} erg s^{-1} cm^{-2}	2.0 ± 0.1	0.8 ± 0.1
$F_{\mathrm{[O\ II]}\lambda\lambda3727,3729}$	10^{-19} erg s^{-1} cm^{-2}	18.0 ± 1.1	2.7 ± 0.6
$F_{\mathrm{[O\ III]}\lambda4363}$	10^{-19} erg s^{-1} cm^{-2}	7.2 ± 1.1	2.9 ± 0.5
$\mathrm{H}\gamma/\mathrm{H}\beta$		0.45 ± 0.03	0.54 ± 0.04
A_V		$0.3^{+0.6}_{-0.3}$	0
SFR	log[M$_\odot$ yr^{-1}]	1.73 ± 0.03	1.17 ± 0.02
T_e([O III])	10^4 K	1.6 ± 0.2	1.8 ± 0.4
n_e	cm^{-3}	790^{+410}_{-250}	1000 (assumed, see Section 4.2.3)
12+log(O/H)	Strong-line	*7.81 ± 0.11* (see Section 4.3)	7.41 ± 0.15
12+log(O/H)	Direct T_e	$7.90^{+0.30}_{-0.21}$	$7.70^{+0.22}_{-0.20}$

Notes. Upper segment: Δv represents the velocity offset of the broad component relative to the narrow component. Lower segment: derived integrated properties of our targets. The strong-line metallicities are estimated using all five diagnostic ratios shown in Table 1. The strong-line metallicity of ID6355 may be affected by AGN ionization, as discussed later in Section 4.3. Note that A_V is quoted as 0 for ID10612 as the $\mathrm{H}\gamma/\mathrm{H}\beta$ ratio indicates no dust in this galaxy.

content, though non-negligible extinction is also possible within the uncertainties.

We note that the integrated spectrum of ID10612 exhibits a $\mathrm{H}\gamma/\mathrm{H}\beta$ ratio significantly larger than intrinsic, resulting in an unphysical A_V; such anomalous Balmer line ratios in early galaxies have been shown in simulations (e.g. W. McClymont et al. 2025a) and can also be seen in stacks of Type-II AGN spectra (J. Scholtz et al. 2025d). The anomalous line ratios cannot be explained by dust attenuation alone, indicating that density-bound nebulae depart from Case-B physics. Furthermore, Case-B ionization is highly dependent on particular temperatures and densities, and may only apply to specific regions within a galaxy. Hence, we can attribute the anomalous Balmer ratio in this galaxy to peculiar gas conditions; non-subtracted stellar continuum or other contaminants are unlikely to play a role due to the weakness of the continuum. As we cannot estimate A_V directly in ID10612 from the Balmer line ratios, we assume no dust, consistent with the findings of M. Curti et al. (2023) and S. Tacchella et al. (2023). A significant caveat to this approach arises as it does not allow correction for absorption of ionizing photons by dust before they ionize hydrogen, but this will have a negligible effect on our results at the low A_V values we find.

4.2.2 Star formation rates

Star formation rates (SFRs) are typically calculated from Hα luminosity, but this emission line is outside of the NIRSpec/IFU wavelength range at the redshifts of our targets. In this work, we instead employ dust-corrected Hβ luminosity as a proxy for Hα luminosity, based on the case-B intrinsic ratio between the lines ($\mathrm{H}\alpha/\mathrm{H}\beta = 2.86$; D. E. Osterbrock 1989). This ratio is dependent on both temperature and density, and as mentioned in Section 3.2, the Balmer-line ratio does not trace the entire dust content of the galaxy. However, due to the low dust attenuation we observe in these galaxies, we deem this approach sufficiently reliable for our purposes.

To ensure we account for SF in the full extent of each galaxy, we extract integrated spectra from 0.5 and 0.4 arcsec radius circular apertures for ID6355 and ID10612, respectively (see Fig. B1 in Appendix B), and calculate the integrated flux of the Hβ narrow-line component. After correcting for dust attenuation, we estimate $L_{\mathrm{H}\beta}$ by combining these results with luminosity distance as estimated from our fitted redshifts. We ultimately estimate SFRs by adapting the Hα–SFR relation from R. C. Kennicutt & N. J. Evans (2012),

$$\log_{10}(\mathrm{SFR}\ [\mathrm{M}_\odot\ \mathrm{yr}^{-1}]) = \log_{10}(2.86 \times L_{\mathrm{H}\beta}\ [\mathrm{erg\ s}^{-1}]) - 41.27. \quad (4)$$

We thus identify overall lensing-corrected SFRs of $\log(\mathrm{SFR}\ \mathrm{M}_\odot\ \mathrm{yr}^{-1}) = 1.73 \pm 0.03$ and 1.17 ± 0.02 in ID6355 and ID10612, respectively. We note that the Balmer-to-SFR conversion was calibrated for normal SFGs and solar metallicities, meaning that a non-zero ionizing photon escape fraction, or the presence of an AGN (as is likely the case for our targets), will introduce further systematic errors $\gtrsim 0.15$ dex in the measured SFRs (i.e. R. C. Jr Kennicutt 1998; R. L. Theios et al. 2019).

4.2.3 Electron temperature, density, and integrated metallicity

In ID6355, the individual [O II]$\lambda\lambda$3727, 3729 and [O III]λ4363 emission lines are each detected with SNR > 3, so electron density (n_e) and temperature (T_e) may be measured directly us-

Downloaded from https://academic.oup.com/mnras/article/546/3/stag094/8426291 by guest on 31 March 2026

ing PyNeb. We estimate a galaxy-integrated electron density of 790^{+410}_{-250} cm^{-3} in ID6355, consistent with other densities measured at high-z, i.e. $n_e \sim 300 - 1000$ cm^{-1} (Y. Isobe et al. 2023; C. Marconcini et al. 2024; J. Scholtz et al. 2025c). We also measure an electron temperature of $(1.6 \pm 0.2) \times 10^4$ K.

However, even in the galaxy-integrated spectrum of ID10612, the individual [O II]λλ3727, 3729 lines are not detected with sufficient SNR for direct calculation of electron density to be possible. Instead, we assume n_e of this galaxy is comparable to ISM electron densities found by studies of other *JWST* galaxies at $z \sim 7 - 9$, i.e. $n_e \sim 1000$ cm^{-3} (Y. Isobe et al. 2023), leveraging this assumed electron density together with the measured [O III]λ4363/[O III]λ5007 ratio to calculate T_e. Hence, we estimate an electron temperature of $(1.8 \pm 0.4) \times 10^4$ K in ID10612. We note that measured T_e does not have a strong dependence on the choice of density estimation provided $n_e \lesssim 1000$ cm^{-3}, so assuming a lower n_e has a negligible impact on the measured direct-T_e metallicity.[3]

We present the galaxy-integrated metallicities in Table 3. We measure strong-line metallicities of $12 + \log(O/H) = 7.81 \pm 0.11$ ($0.13^{+0.04}_{-0.03}$ $Z_\odot$) and 7.41 ± 0.15 ($0.05^{+0.02}_{-0.01}$ $Z_\odot$) in the central region ($r \sim 1.25$ kpc) of ID6355 and ID10612, respectively. Additionally, we estimate the overall direct-T_e metallicity of ID6355 as $7.90^{+0.30}_{-0.21}$ ($0.16^{+0.11}_{-0.08}$ $Z_\odot$). For ID10612, the assumption of $n_e \sim 1000$ cm^{-3} yields a direct-T_e metallicity of $7.70^{+0.22}_{-0.20}$ (0.10 ± 0.05 $Z_\odot$). We note that for each galaxy, both methods yield values of metallicity consistent within the associated errors.

4.3 Metallicity profiles

Having measured the integrated chemical properties of the two galaxies, we now utilize our spatially resolved detection of the emission lines (Figs 2 and 3) to study the spatial variation of their metallicities.

We first investigate the variation of metallicity on a spaxel-by-spaxel basis, utilizing the PSF-matched cubes to present strong-line metallicity maps of ID6355 and ID10612 in Figs 5(a) and (b), respectively. The metallicity variation is irregularly distributed in both galaxies (Fig. 5). At the same time, the error in each metallicity for a given spaxel (~ 0.2 dex) is comparable to the magnitude of metallicity variation across the entire galaxy, indicating that both galaxies have flat metallicity profiles overall. We stress that these maps should be interpreted with caution, as the strong-line metallicity calibrations are based on observations at $z \sim 2 - 3$ (E. Cataldi et al. 2025) and may not be reliable at $z \sim 7.6$. Furthermore, as previously discussed (see Section 3.2), the presence of an AGN in a galaxy will affect its measured line ratios and hence also any inferred strong-line metallicity (M. Curti et al. 2017, 2020a; N. Kumari et al. 2021), meaning these maps do not necessarily trace metallicity variation alone.

A more robust approach lies in calculating metallicity gradients using radially binned spectra. We choose to radially bin spaxels in elliptical annuli uniformly spaced along the semimajor axis (width ~ 0.08 arcsec, see Fig. 5), obtaining spectra with higher SNR than available from individual spaxels. A different choice of bin (e.g. non-uniformly spaced) does not significantly impact our science results. The elliptical bins were defined using the corresponding position angle and ellipticity of each galaxy, as obtained by morphological fitting (Table 2), and flux uncertainties were appropriately combined during the binning process. Once again, we utilize all five diagnostic emission-line ratios from Table 1, only calculating the metallicity in a particular annulus if all necessary emission lines are detected at SNR > 3. Metallicities are measured as a function of the distance along the elliptical semimajor axis, and we present these gradients in Fig. 6. We measure strong-line metallicity gradients of -0.01 ± 0.01 and -0.00 ± 0.02 dex kpc^{-1} in ID6355 and ID10612, respectively (see the panels a and c of Fig. 6), consistent with both galaxies having flat metallicity gradients. However, it must again be stressed that calculating strong-line metallicities involves the inherent assumption that observed photoionization is driven by SF. The AGN present in ID6355 may affect observed line ratios independently of metallicity, with implications for its inferred strong-line metallicity gradient. Hence, direct-T_e metallicity gradients would offer a better probe of the metallicity variation in ID6355.

In ID6355, there is sufficiently good detection of [O II]λλ3727, 3729 (SNR > 3 for each line in the doublet) to map electron density in concentric annuli around the centre of the galaxy, though the region we can derive direct-T_e within is limited by the spatial extent of [O III]λ4363 detection (see Fig. 2). When inspecting each annulus-binned spectrum, we identified a small feature blueward of [O III]λ4363, which grows more prominent and contaminates the [O III]λ4363 emission at larger radii. We rule out [Fe II] emission as a cause of this feature, and determine it is most likely caused by a residual outlier that was missed by the data reduction pipeline. Though we masked out the wavelength channels corresponding to this residual feature, it is only possible to avoid its associated [O III]λ4363 contamination and investigate the direct-T_e metallicity gradient on ~ 1 kpc scales. We present the calculated direct-T_e metallicity profile of ID6355 in Fig. 6(b); we identify a negative gradient of -0.11 ± 0.03 dex kpc^{-1}, in tension with the flat gradient found by strong-line measurements; this tension will be discussed further in Section 6.2.

5 GALAXY KINEMATICS

5.1 Kinematical maps

We present an overview of the narrow- and broad-component [O III]λ5007 kinematics in Figs 7(a) and (b). We include integrated [O III]λ5007 flux and velocity dispersion maps of each component (σ_{nar} and σ_{broad}, respectively), as well as the narrow-line relative velocity ($v_{nar,rel}$) and the velocity offset between the components (Δv).

While several different lens models for the SMACS J0723.3−7327 cluster have been published (G. B. Caminha et al. 2022; M. Pascale et al. 2022; G. Mahler et al. 2023), these models yield consistent magnification factors of $\mu \sim 1.2 - 1.7$ for our targets, and we conclude that overall lensing factors of this magnitude would have a negligible influence on the inferred galaxy kinematics (e.g. S. Arribas et al. 2024; G. C. Jones et al. 2024b). Hence, an exploration of the effect lensing model choice might have on the systematics introduced to estimated kinematical properties is beyond the scope of this paper.

Figs 7(a-ii) and (b-ii) show that the broad component in each galaxy is spatially extended beyond the size of the PSF ($r \sim 1$ kpc) and centrally concentrated. In ID6355, there is a ~ 0.1 arcsec (~ 0.5 kpc) offset between the narrow and broad [O III]λ5007

[3] Assuming $n_e \sim 790$ cm^{-3}, i.e. comparable to the density of ID6355, results in changes of ~ 0.01 dex for the inferred T_e and direct-T_e metallicity of ID10612, insignificant relative to the inferred uncertainties).

Downloaded from https://academic.oup.com/mnras/article/546/3/stag094/8426291 by guest on 31 March 2026

flux centroids, while the two components' flux centroids spatially coincide in ID10612. The velocity offsets, Δv, between the narrow and broad components are fairly small (< 100 km s^{-1}) in both galaxies. The fitted velocity dispersion is also significantly higher for the broad component than for the narrow component, as can be seen from a comparison of panels (v) and (vi) in Figs 7(a) and (b).

From the wavelength resolution of the cubes and the mean [O III]λ5007 SNR of individual pixels, we estimate the velocity resolution of our observations as ~ 15 km s^{-1}. From Fig. 7(a-iii), we thus identify a resolved asymmetric velocity gradient in ID6355, but Fig. 7(b-iii) shows there is no clearly resolved rotation in ID10612. Although these galaxies are not rotating axisymmetric discs, we can estimate a constraint on the projected rotational velocities ($v_{\rm obs}$) in each galaxy. For ID6355, this is done by calculating the average of the maximum and minimum $v_{\rm nar,rel}$, as identified at $R_{\rm e}$ in the $v_{\rm nar,rel}$ map. As ID10612 lacks a resolved velocity gradient, we instead estimate the upper bound on its projected rotational velocity as the resolution of our observations, i.e. 15 km s^{-1}. However, $v_{\rm obs}$ must be corrected to account for galaxy inclination, using

$$v_{\rm rot} = v_{\rm obs}/\sin(i), \tag{5}$$

where $v_{\rm rot}$ is the deprojected rotational velocity. We therefore calculated $v_{\rm rot}$ at the effective radius in ID6355 and ID10612 as 65 ± 26 and < 17 km s^{-1} respectively.

To measure the intrinsic velocity dispersion σ, free of resolved motions, we adopt an approach similar to that of E. Wisnioski et al. (2015), measuring the velocity dispersion of the narrow component in the outer regions of the galaxies. This approach reduces the effect of beam smearing, which mainly affects the central region and can be significant when a galaxy has a pronounced velocity gradient (as is the case for ID6355). Using the galaxy-integrated spectra, we measure intrinsic velocity dispersions of 103 ± 40 and 48 ± 11 km s^{-1} in ID6355 and ID10612, respectively.

We assess the relative importance of rotational and dispersional support in each galaxy through the ratio $v_{\rm rot}/\sigma$, measured within the effective radius $R_{\rm e}$. We measure $v_{\rm rot}/\sigma$ as 0.66 ± 0.36 and < 0.36 in ID6355 and ID10612, respectively, indicating that ID6355 exhibits a small degree of rotational support, while ID10612 is entirely dispersion-dominated. Our observation that ID6355, the higher mass of our two galaxies, is also the galaxy exhibiting more rotational support, is as expected from the results of studies at Cosmic Noon (e.g. E. Wisnioski et al. 2015).

In Fig. 8, we compare our $v_{\rm rot}/\sigma$ to those from other ionized gas studies across cosmic time. Previous studies of ionized (E. Parlanti et al. 2023; A. Graaff et al. 2024; S. Arribas et al. 2024; A. L. Danhaive et al. 2025) and cold (L. E. Rowland et al. 2024) gas at high redshift have indicated that highly turbulent systems such as our targets are not uncommon at early cosmic times, though we note that cold gas kinematics are known to be different from those of ionized gas. Our results are in tension with SERRA simulations of ionized gas for galaxies in a stellar mass range similar to that of our targets (M. Kohandel et al. 2024), which predict higher $v_{\rm rot}/\sigma$ across early cosmic times. We instead find our results are consistent with an expected increase in σ and decrease in rotational support towards early cosmic times, as predicted by some other simulations such as TNG (A. Pillepich et al. 2019) and now observed in many galaxies at $z \gtrsim 4$ (A. L. Danhaive et al. 2025).

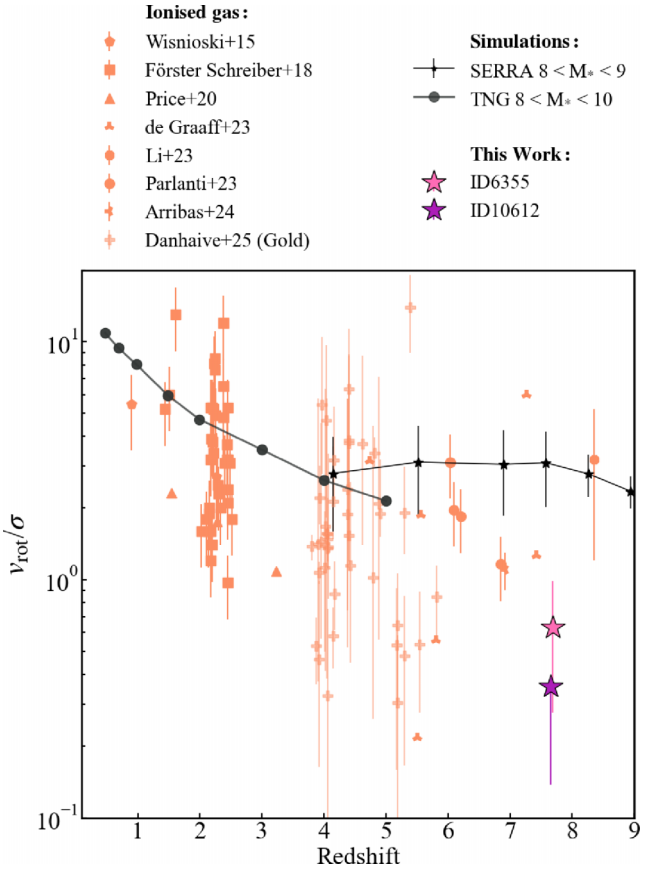

Figure 8. The evolution of $v_{\rm rot}/\sigma_{\rm v}$, as traced by ionized gas, across cosmic time. We compare ID6355 and ID10612 to a compilation from the literature, including observations of ionized gas: *JWST*/NIRCam (Z. Li et al. 2023; gold sample from A. L. Danhaive et al. 2025), ground-based IFU (E. Wisnioski et al. 2015; N. M. Förster Schreiber et al. 2018), MOSFIRE (S. H. Price et al. 2020), ALMA $z \sim 6$ (E. Parlanti et al. 2023), NIRSpec (A. Graaff et al. 2024; S. Arribas et al. 2024); and simulations: ILLUSTRIS-TNG (A. Pillepich et al. 2019) and SERRA (M. Kohandel et al. 2024). ID10612 only has a lower error bar in this plot, as its estimated rotational velocity is an upper limit.

5.2 Dynamical masses

To constrain the dynamical mass of our targets, we follow the same approach as other works (e.g. H. Übler et al. 2023; S. Carniani et al. 2025), using the relation from A. der Wel et al. (2022):[4]

$$M_{\rm dyn} = \beta(n)K(q)\frac{\sigma_*^2 R_{\rm e}}{G}, \tag{6}$$

where σ_* is the stellar velocity dispersion. $\beta(n) = 8.87 - 0.831n + 0.0241n^2$ and $K(q) = \left[0.87 + 0.38e^{-3.71(1-q)}\right]^2$ are correction factors for galaxy profile and inclination, following M. Cappellari et al. (2006) and A. der Wel et al. (2022), respectively. σ_* is inferred from σ using the best-fitting relations from R. Bezanson et al. (2018), $\sigma_* \simeq 1.26 \times \sigma$. $M_{\rm dyn}$ represents twice the mass inside the sphere of radius $R_{\rm e}$ (M. Cappellari et al. 2006); in the following analysis, we treat $M_{\rm dyn}$ as the total mass, even though

[4]We note that this approach was calibrated for the stellar kinematics of massive ($M_* \sim 10^9 - 10^{10}$ M$_\odot$) galaxies at $z \sim 0.8$, but other calibrations provide similar answers, within ~ 0.3 dex (C. Marconcini et al. 2024).

Downloaded from https://academic.oup.com/mnras/article/546/3/stag094/8426291 by guest on 31 March 2026

Table 4. Summary of derived dynamical properties of each galaxy, along with bootstrapped errors quoted at the 68 per cent confidence interval. v_{rot} been corrected for galaxy inclination; see Equation (5). For the comparison of dynamical to stellar mass, we note that M. Curti et al. (2023) measure stellar masses of $\log(M_*/M_\odot) = 8.72 \pm 0.04$ and 8.08 ± 0.04 in ID6355 and ID10612, respectively.

Property	Unit	Value	
		ID6355	ID10612
v_{rot}	km s^{-1}	65 ± 26	< 17
σ	km s^{-1}	103 ± 40	48 ± 11
σ_*	km s^{-1}	130 ± 50	61 ± 14
v_{rot}/σ		0.63 ± 0.36	< 0.36
$\log_{10}(M_{dyn}/M_\odot)$		$10.6^{+0.2}_{-0.6}$	$9.9^{+0.2}_{-0.3}$
M_*/M_{dyn}		0.013 ± 0.010	0.015 ± 0.007
v_{esc}	km s^{-1}	480 ± 190	210 ± 50

it represents an extrapolation and the true total mass can thus be much larger.

We report measured dynamical masses of ID6355 and ID10612 as $\log_{10}(M_{dyn}/M_\odot) = 10.6^{+0.2}_{-0.6}$ and $9.9^{+0.2}_{-0.3}$, respectively (see Table 4). It is also interesting to investigate the M_*/M_{dyn} ratio, as this gives an indication of the gas (and dark matter) fraction in a galaxy. Taking M_* as measured by M. Curti et al. (2023, see the caption of Table 4), we find $M_*/M_{dyn} = 0.013 \pm 0.010$ and 0.015 ± 0.007 in ID6355 and ID10612, respectively. These low ratios of stellar to dynamical mass indicate both galaxies have high gas fractions and/or high dark matter fractions in their central regions, which have also been found for other distant, low-mass galaxies (A. Graaff et al. 2024; A. L. Danhaive et al. 2026). In galaxies with low stellar masses (i.e. $\log(M_*/M_\odot) \leq 9.5 - 10$), high gas fractions such as these combine with shallow potential wells to promote central starbursts. Gas inflows to the central regions (A. Dekel & A. Burkert 2014; K. El-Badry et al. 2016; S. Tacchella et al. 2016; P. F. Hopkins et al. 2023), and outflows triggered by SF (e.g. S. Carniani et al. 2024b), disrupt disc settling, and inject turbulence into the ISM. Low-mass galaxies are also more unstable to disruption from gravitational instabilities. The interplay of these disruptive mechanisms can help explain the low degree of rotational support measured in our two galaxies and other galaxies in the early Universe (A. L. Danhaive et al. 2025).

5.3 Identification of high-velocity gas

By mapping the kinematics of the [O III]λ5007 emission line in each galaxy, we have identified a resolved velocity gradient in ID6355 and a lack of resolved velocity gradient in ID10612 [see Figs 7(a-iii) and (b-iii), respectively]. We have also found broad components in both ID6355 and ID10612, which are redshifted relative to their narrow-line counterparts. We now seek to disentangle the broad components in each galaxy from systemic disc emission, to show clearly that the broad components are not associated with galactic rotation but rather have a separate kinematical origin, such as an outflow or merger.

To more clearly illustrate the motion of gas, we create velocity channel maps for each galaxy (see Figs 9 and 10) by collapsing the IFU cubes into velocity channels of 100 km s^{-1}, centred around the observed peak of [O III]λ5007 emission. If these galaxies exhibit pure rotation, we would expect the peak flux to be symmetric across the 0 km s^{-1} boundary in Figs 9 and 10. However, we instead observe a faint flux in the high velocity ($\sim 200 - 400$ km s^{-1}) channels of both galaxies, which is not noticeably present in the corresponding low velocity channel, indicating a discrepancy. The additional broad kinematical component in these galaxies can manifest as an asymmetry in the channels such as we observe here, as any broad component such as outflow or merger is generally complex and affected by attenuation by ISM in the disc.

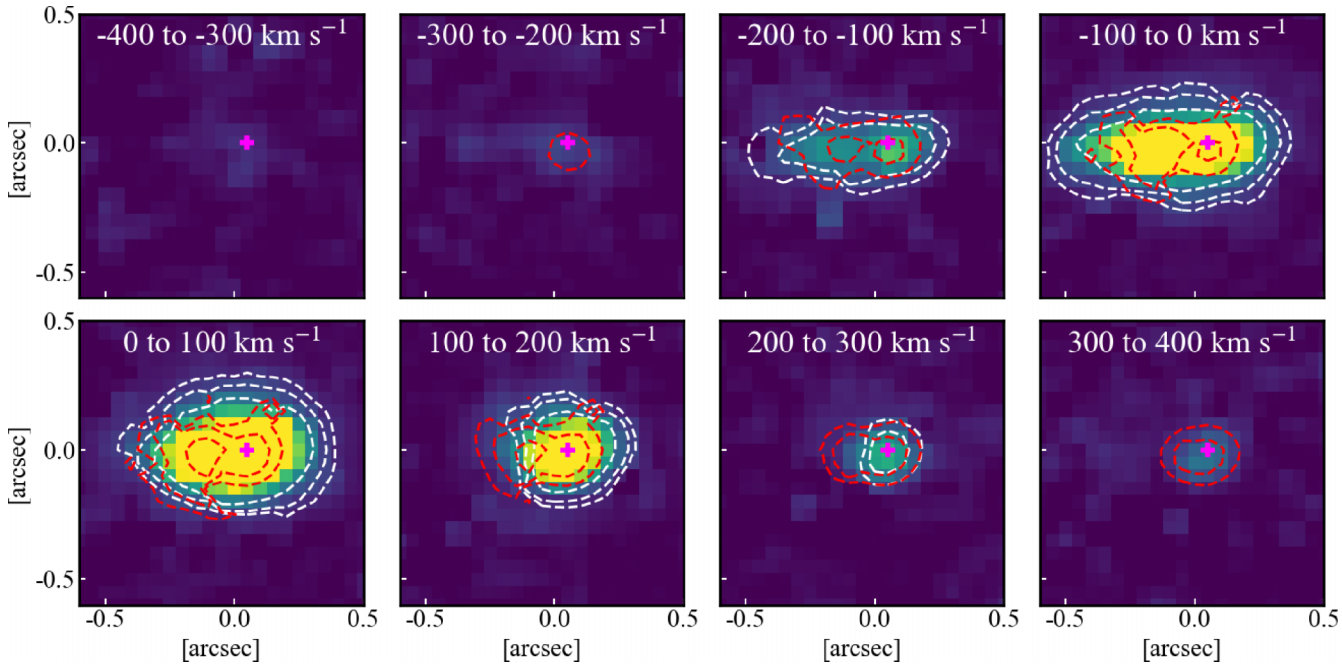

Figure 9. Velocity channel maps of ID6355, created by collapsing the spectral flux into 100 km s^{-1} relative velocity channels centred on the observed peak of the [O III]λ5007 emission line. The [O III]λ5007 flux centroid is shown as a magenta cross in each subplot. The dashed contours in white and red correspond to the 3σ, 5σ, and 10σ flux levels of the fitted narrow and broad components, respectively, in each channel.

Downloaded from https://academic.oup.com/mnras/article/546/3/stag094/8426291 by guest on 31 March 2026

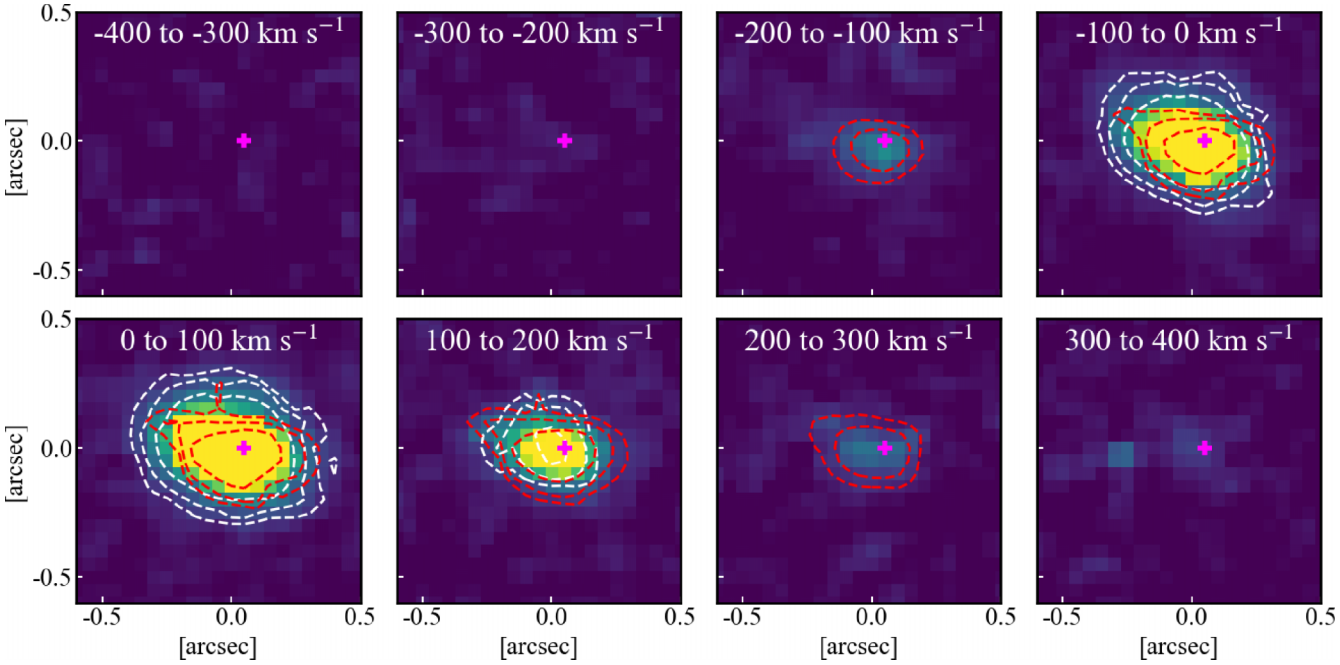

Figure 10. Velocity channel maps of ID10612, created by collapsing the spectral flux into 100 km s^{-1} relative velocity channels centred on the observed peak of the [O III]λ5007 emission line. The [O III]λ5007 flux centroid is shown as a magenta cross in each subplot. The dashed contours in white and red correspond to the 3σ, 5σ, and 10σ flux levels of the fitted narrow and broad components, respectively, in each channel.

In Figs 9 and 10, we additionally show the contours of fitted narrow and broad component flux in each velocity channel, plotted at the 1σ, 3σ, and 5σ confidence levels. In each galaxy, the broad component of the [O III]λ5007 line is asymmetrically distributed about the central wavelength, contributing significantly to the high velocity ($\sim 200-400$ km s^{-1}), redshifted component. As the broad flux falls well outside what we can reasonably attribute to the galactic rotation, we conclude that these broad components arise due to a second kinematical component in each galaxy.

5.4 Origin of the broad component

Across the previous sections, we have presented evidence for an additional high-velocity (>200 km s^{-1}), non-rotating kinematical component in the [O III]λ5007 emission-line-based kinematics of both galaxies (see Figs 1, 7, 9, and 10). We will now discuss the possible origin of these broad components.

S. Tacchella et al. (2023) analysed the NIRCam photometry of these galaxies, finding that both have shown a recent increase in SFR. They further identified both galaxies as having complex morphologies consisting of multiple components, suggesting that their recent increases in SFR are driven by *in-situ* gravitational instabilities or mergers. In fact, enhanced merger rates are expected in protocluster environments like the one which hosts our target galaxies (L. C. Marcelin et al. 2025). Our measured broad components are also consistent with a merger, as there are small spectral (< 100km s^{-1}) and spatial (< 0.2 arcsec) separations between the narrow and broad components in each object. However, it should be pointed out that the galaxies were shown to be clumpy in the UV NIRCam filters, suggesting bursty SF rather than a merger origin. Additionally, we do not see a multiply peaked [O III]λ5007 or Hβ flux distribution in our spatial maps as is typically found in mergers (e.g. G. C. Jones et al. 2024b).

Interestingly, the broad component in both galaxies is redshifted relative to the narrow component; this indicates the gas is moving along the line of sight away from us, suggesting an inflow of gas. However, there are two significant problems with this explanation. First, we have determined both galaxies to have low dust content (based on measurements of Hγ/Hβ; see Section 4.2.1), rendering it unlikely that a significant [O III]λλ4959, 5007 blue wing is present but dust-obscured. Secondly, in the case of an inflow, we would expect to see the broad component correspond to nearly pristine gas with [O III]λ5007/Hβ < 1 (E. Vanzella et al. 2023; K. Nakajima et al. 2025; T. Y.-Y. Hsiao et al. 2025; R. Maiolino et al. 2025a). However, we note that our measured broad components have [O III]λ5007/Hβ ratios of 4.0 ± 0.9 and 8.6 ± 2.3 in ID6355 and ID10612, respectively, significantly higher than expected for pristine inflowing gas.

Another, more likely, explanation for the observed broad component is an outflow. Indeed, Y. Xu et al. (2025) utilized the MSA spectra of ID6355 and ID10612 to identify their broad components and characterized them as outflows. The broad component velocities we now infer are high ($\gtrsim$ 250 km s^{-1}), as are the velocity dispersions of both the narrow and broad components (Table 4), more suggestive of gas that is highly turbulent and re-energized in some way, possibly from feedback processes. Furthermore, Fig. 9 indicates the broad component in ID6355 does contribute to high-velocity gas at −300 to −200 km s^{-1}, as we might traditionally expect for an outflow. The redshifted nature of the broad component could arise due to outflow orientation, but due to our small sample size, we cannot distinguish whether redshifted outflow components are a systemic property of early galaxies like our targets, or whether we have simply managed to identify this population by chance. Regardless, purely redshifted outflows have already been observed as part of lower redshift studies such as the KASHz survey at Cosmic Noon, where ∼ 16 per cent of outflows are found to be redshifted rather than blueshifted (C.

Downloaded from https://academic.oup.com/mnras/article/546/3/stag094/8426291 by guest on 31 March 2026

Table 5. Summary of outflow properties, estimated by fitting the two-Gaussian model (Section 3.1) to an integrated spectrum extracted from the 'outflow region' of each galaxy, along with bootstrapped errors quoted at the 68 per cent confidence interval. $M_{\rm out}$ is calculated based on the direct-$T_{\rm e}$ metallicity of each galaxy (see Table 3). $r_{\rm out}$ and $M_{\rm out}$ have been corrected for lensing.

Property	Unit	ID6355	ID10612
$\sigma_{\rm broad,deconv}$	km s^{-1}	210 ± 20	120 ± 10
$\Delta v_{\rm outflow}$	km s^{-1}	92 ± 23	30 ± 10
$r_{\rm out}$	kpc	$0.95^{+0.16}_{-0.20}$	$0.73^{+0.14}_{-0.18}$
$v_{\rm out}$	km s^{-1}	512^{+83}_{-84}	255^{+18}_{-27}
$v_{\rm out}/v_{\rm esc}$		1.06 ± 0.45	1.23 ± 0.31
$M_{\rm out}$	10^6 M$_\odot$	$8.2^{+10.4}_{-3.5}$	$7.4^{+7.0}_{-2.9}$
$\dot{M}_{\rm out}$	M$_\odot$ yr^{-1}	14^{+18}_{-6}	8^{+11}_{-3}
η		$0.3^{+0.3}_{-0.1}$	$0.4^{+0.5}_{-0.2}$

M. Harrison et al. 2016; J. Scholtz et al. 2020). A larger sample of similar targets would be required to statistically determine whether red-shifted outflows are common at high-z.

Robustly identifying the origin of a broad component is not straightforward at such high redshifts, and is complicated further by the low masses of our targets. With multiphase or higher resolution observations, it may be possible to conclusively distinguish between the different scenarios, but currently we work within the limitations of our data. Given the high outflow velocity ($\sim$ 500 km s^{-1}) and central concentration of the broad kinematical component in ID6355, we conclude that this component is not part of an inflow or a merger. As such, taking into consideration the caveats discussed above, we attribute the broad component to an outflow in ID6355. On the other hand, interpreting the broad component in ID10612 is more challenging. The lower outflow velocity of 255 km s^{-1}and lack of settled kinematics (see Section 5) in this galaxy make the outflow interpretation difficult. Hence, the broad component could be an artefact of the complex kinematics of this object; we can note the obvious 'footprint' of the broad component visible in Fig. 7(b-v) as evidence of the difficulties of disentangling the kinematical components in this galaxy. Therefore, from now on we tentatively attribute the broad component of ID10612 to an outflow.

5.5 Outflow properties

Having identified evidence that the broad component in each galaxy arises from an ionized gas outflow, we now estimate the associated outflow properties. We first extract an integrated spectrum from the 'outflow region' of each galaxy, as identified in Figs 7(a-ii) and (b-ii), where the broad component of [O III]λ5007 emission is detected with SNR > 5. To determine the velocity of the outflowing gas ($v_{\rm out}$), we use the prescription from D. S. Rupke, S. Veilleux & D. B. Sanders (2005):

$$v_{\rm out} = |v_{\rm broad} - v_{\rm narrow}| + 2\sigma_{\rm broad,deconv}, \quad (7)$$

where $|v_{\rm broad} - v_{\rm narrow}| = \Delta v$ is the velocity offset between the peaks of the broad and narrow components. $\sigma_{\rm broad,deconv}$ is the velocity dispersion of the broad component (measured as 210 ± 20 and 120 ± 10 km s^{-1} in ID6355 and ID10612, respectively; Table 5), which has been deconvolved with the instrumental line-spread function $\sigma_{\rm LSF}$ (i.e. $\sigma^2_{\rm broad,deconv} = \sigma^2_{\rm broad} - \sigma^2_{\rm LSF}$). We adopt this method as it guarantees outflow velocities are not significantly dependent on the inclination of the outflow cone with respect to the line of sight (D. S. Rupke et al. 2005; F. Fiore et al. 2017). We estimate outflow velocities of 512^{+83}_{-84} and 255^{+18}_{-27} km s^{-1} for ID6355 and ID10612, respectively, which are slow compared to the outflow velocities one might typically expect for AGN-driven outflows, $\sim 400 - 3500$ km s^{-1} (e.g. R. L. Davies et al. 2020). We additionally note that $v_{\rm out}$ should be treated as an upper limit, as only a small fraction of outflowing material would be moving with this high velocity.

We compare the outflow velocity of our sources to those of other *JWST* spectroscopically identified outflows (traced by Hα or [O III]λ5007, i.e. ionized gas) across cosmic time in Fig. 11; our results are consistent with other [O III]-detected outflows at $z \sim 7 - 8$ in having outflow velocities < 1000 km s^{-1}. This figure also includes three QSOs observed with NIRSpec/IFS at high-z (e.g. M. A. Marshall et al. 2023), showing that high-luminosity or massive sources can show dramatically faster outflows even at early cosmic times (M. Brazzini et al. 2025). This is in contrast to the lower mass regime probed by our targets, where we expect to see lower velocity outflows. Our results show outflow velocities consistent with those in SFGs, hinting at bursty SF as a potential driver for the outflows.

Over time, outflows can have a significant effect on a galaxy's evolution, either by evacuating the gas into the circumgalactic medium (CGM) or by heating the CGM and thereby inhibiting future gas accretion (S. Brownson et al. 2019; G. C. Jones et al. 2023; J. S. Bennett et al. 2024). We assess the long-term impact of our detected outflows by comparing the measured outflow velocity to the escape velocity of the host galaxy. From our estimate of $M_{\rm dyn}$ (see Section 5.2), we calculate the escape velocity $v_{\rm esc}$ as

$$v_{\rm esc} = \sqrt{\frac{2GM_{\rm dyn}}{R_{\rm e}}}. \quad (8)$$

We find $v_{\rm out}/v_{\rm esc}$ ratios of 1.06 ± 0.45 and 1.23 ± 0.31 for ID6355 and ID10612, respectively, indicating that $v_{\rm out} \gtrsim v_{\rm esc}$ for the highest velocity outflowing gas in both of our targets. While only part of the outflowing gas may escape the gravitational potential of the halo, this may enrich the CGM with metals and additionally suppress SF over long time-scales, as gas is gradually depleted from the galaxy. We compare the relationship of the $v_{\rm out}/v_{\rm esc}$ ratio to stellar mass both in our targets and in samples selected from the literature in the left-hand panel of Fig. 12 (see Section 6.1 for further discussion).

We estimate the mass of outflowing gas, $M_{\rm out}$, directly from the dust-corrected luminosity $L^{\rm corr}_{\rm [O\,III]}$ of the broad component of [O III]λ5007 (see e.g. S. Carniani et al. 2015), using

$$M_{\rm out} = 0.8 \times 10^8 \left(\frac{L^{\rm corr}_{\rm [O\,III]}}{10^{44}\ {\rm erg\ s^{-1}}}\right)\left(\frac{Z_{\rm out}}{Z_\odot}\right)^{-1}\left(\frac{n_{\rm out}}{500\ {\rm cm^{-3}}}\right)^{-1} {\rm M_\odot}, \quad (9)$$

where $Z_{\rm out}$ and $n_{\rm out}$ are the metallicity and electron density of the outflowing gas, respectively. However, diagnostic emission lines necessary to measure $n_{\rm e}$ and direct-$T_{\rm e}$ metallicity are too faint to be detected in our observed outflows, and assumptions must be made. Some studies of outflows at high-z (e.g. A. Concas et al. 2022; S. Carniani et al. 2024b) assume an outflow electron density of 380 cm^{-3}, the typical value estimated from deep observations of $z \sim 2$ SF-driven outflows (N. M. Förster Schreiber et al. 2019). However, we opt for a more conservative approach, setting the outflow density for both galaxies as $n_{\rm e} = 1000$ cm^{-3}, the median ISM density of $z \sim 7 - 9$ *JWST* galaxies as found by Y. Isobe et al. (2023). Additionally, we set $Z_{\rm out}$ as the direct-$T_{\rm e}$ gas-phase

Downloaded from https://academic.oup.com/mnras/article/546/3/stag094/8426291 by guest on 31 March 2026

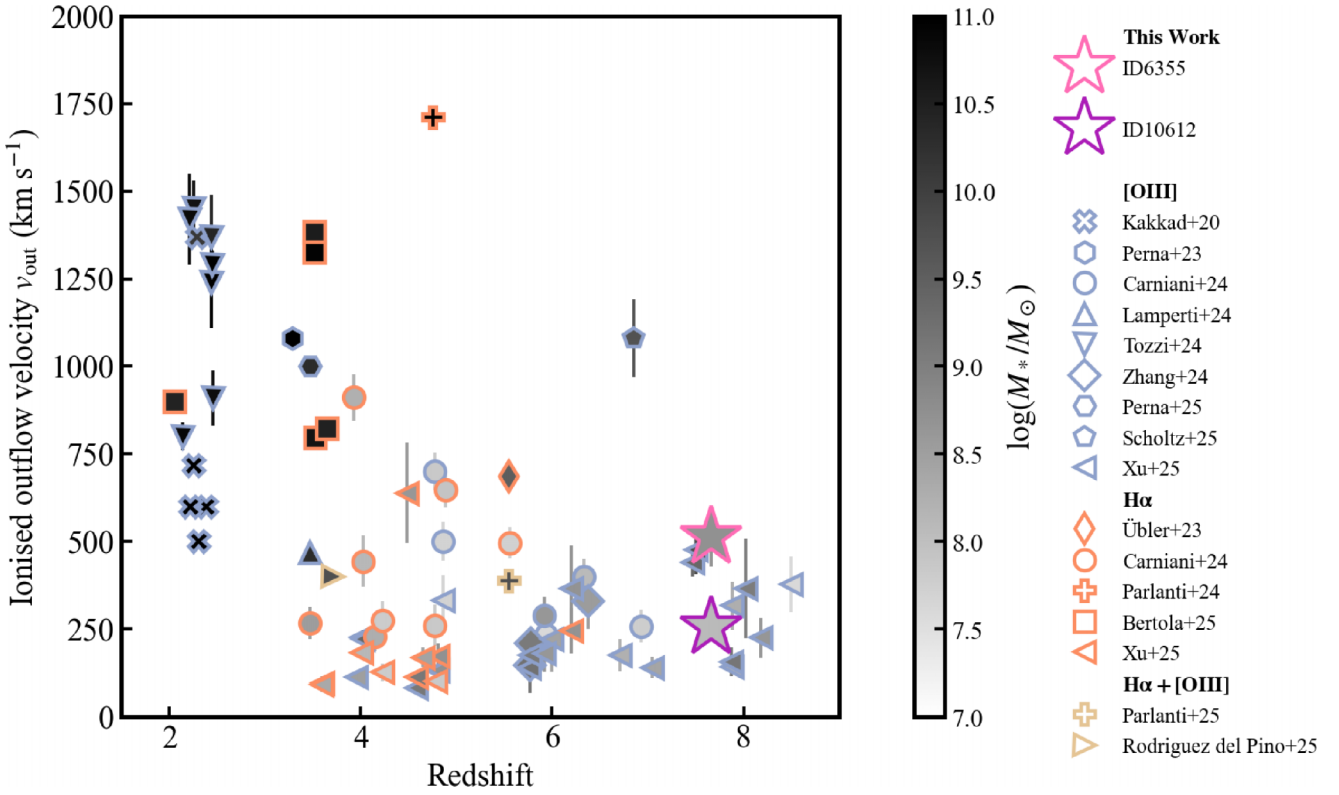

Figure 11. Cosmic evolution of ionized gas outflow velocities measured from rest-frame optical emission lines, with dependence on stellar mass also illustrated. ID6355 and ID10612 are plotted as the pink- and purple-outlined stars, respectively. Points in blue, orange, and yellow outlines correspond to outflows detected in Hα, [O III], or both, respectively. The comparison samples shown in this plot include outflow velocities measured in: low-mass, high-redshift AGN, and SFGs (Y. Zhang et al. 2024; S. Carniani et al. 2024b; Y. Xu et al. 2025); higher mass galaxies and quasars from the GA-NIFS literature (M. Perna et al. 2023; H. Übler et al. 2023; I. Lamperti et al. 2024; E. Parlanti et al. 2024; B. Rodríguez Del Pino et al. 2024; E. Bertola et al. 2025; E. Parlanti et al. 2025; M. Perna et al. 2025; J. Scholtz et al. 2025c); and massive AGN-host galaxies at $z \sim 2$ (D. Kakkad et al. 2020; G. Tozzi et al. 2024).

metallicity of each galaxy[5], i.e $0.16^{+0.11}_{-0.08}$ and $0.10^{+0.06}_{-0.04}$ $Z_\odot$ in ID6355 and ID10612, respectively (see Section 4.2.3).

To estimate mass outflow rates, we adopt the same approach as other high-redshift outflow studies (e.g. S. Carniani et al. 2024b; R. A. Cooper et al. 2025), assuming a uniformly filled conical outflow:

$$\dot{M}_{out} = 3 M_{out} v_{out} / r_{out}, \quad (10)$$

where r_{out} is the extension of the outflow (e.g. R. Maiolino et al. 2012; E. González-Alfonso et al. 2017). This approach also assumes that the outflow rate is constant with time (e.g. D. Lutz et al. 2020). We estimate the outflow extension r_{out} by measuring the area of the outflow region, approximating it as circular, and calculating the corresponding radius; this yields $r_{out} \sim 1$ kpc in each galaxy, comparable with the measured effective radii (see Table 2), and therefore representative of extended outflows.

We estimate the mass outflow rates of our sources to be 14^{+18}_{-6} and 8^{+11}_{-3} $M_\odot yr^{-1}$ in ID6355 and ID10612, respectively, and report the properties of our detected outflows in Table 5. We will further discuss the impact of the outflows in Section 6.3. It should be noted that the measured outflow masses and rates are highly sensitive to the choice of assumptions related to metallicity, electron density, and outflow geometry. For example, we find that assuming the outflow metallicity is closer to solar would decrease the mass outflow rate by a factor of ∼7–10 in both galaxies. Furthermore, assuming a shell rather than filled multiconical outflow geometry would reduce the measured mass outflow rate by a factor of three (D. Lutz et al. 2020). As an additional caveat, we note that [O III]-based energetics are typically underestimated with respect to Hβ-based ones (S. Carniani et al. 2015; F. Fiore et al. 2017; M. Perna et al. 2019), which could also reduce our measured mass outflow rate.

A further way of evaluating outflow impact is through estimating the mass-loading factor (η) of the outflow,

$$\eta = \dot{M}_{out}/SFR, \quad (11)$$

which indicates the primary source of gas consumption in the system. We estimate $\eta = 0.3^{+0.3}_{-0.1}$ and $0.4^{+0.5}_{-0.2}$ in ID6355 and ID10612, respectively, showing that outflows are subdominant to SF in both galaxies. We must be conservative in interpreting η, as the assumptions involved in calculating mass-loading factor, including the caveats discussed above, can have systematic uncertainties of up to ∼ 1 dex (D. Kakkad et al. 2020). Furthermore, we note that η is an instantaneous quantity that can change on time-scales of a few Myr (e.g. Y. Qiu et al. 2021), and hence is not representative of the long-term effect of feedback. We investigate the relationship of η to stellar mass in our targets through comparison to a literature sample in the right-hand panel of Fig. 12 (see Section 6.1 for discussion).

[5]We note as a caveat that outflows are known to be more metal enriched than narrow-line regions (e.g. P. Du et al. 2014).

Downloaded from https://academic.oup.com/mnras/article/546/3/stag094/8426291 by guest on 31 March 2026

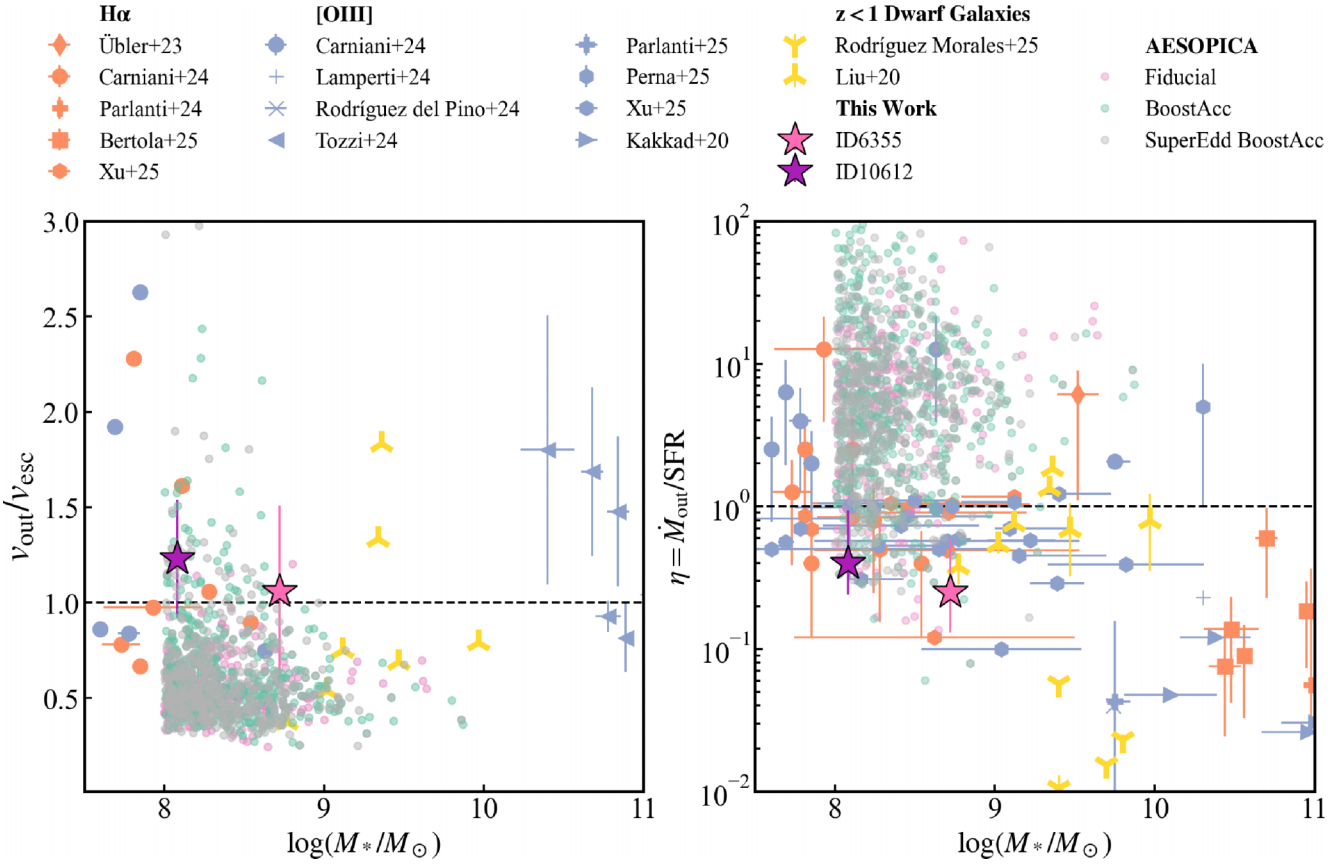

Figure 12. A summary of ionized gas outflow properties across observations and simulations. We compare our results for ID6355 and ID10612 (the pink and purple stars, respectively, in each plot) to outflows in $z > 2$ AGN-host and SFGs (a subsample of the literature shown in Fig. 11), as well as local ($z < 1$) AGN-host dwarf galaxies from W. Liu et al. (2020) and V. Rodríguez Morales et al. (2025). We additionally compare our results to three different modes of the AESOPICA simulations (Koudmani et al., in preparation) of outflows in $z \sim 7.6$ dwarf galaxy AGN: *Fiducial*, boosted accretion (*BoostAcc*), and super-Eddington with boosted accretion (*SuperEdd+BoostAcc*). Left-hand panel: ratio of the ionized gas outflow velocity to escape velocity (v_{out}/v_{esc}) as a function of stellar mass. v_{esc} for our targets have been estimated via calculated dynamical mass as described in Section 5.2. The black dashed line indicates $v_{out}/v_{esc} = 1$. Right-hand panel: mass-loading factor ($\eta = \dot{M}_{out}/SFR$) as a function of stellar mass. The black dashed line indicates $\eta = 1$.

6 DISCUSSION

6.1 Comparison to NIRSpec/MSA integrated measurements

A number of existing studies (e.g. D. Schaerer et al. 2022; J. Brinchmann 2023; J. R. Trump et al. 2023; M. Curti et al. 2023; S. Tacchella et al. 2023; A. C. Carnall et al. 2023a; Y. Xu et al. 2025) have utilized NIRSpec/MSA data from the ERO programme to characterize the two galaxies presented in this study. In this section, we present a brief overview of how our results, obtained from the higher resolution NIRSpec/IFU observations, compare to those from previous studies.

First of all, we discuss SFRs. Previous studies all present measured SFRs that are significantly smaller than our values across both galaxies (J. Brinchmann 2023; K. Nakajima et al. 2023; M. Curti et al. 2023; S. Tacchella et al. 2023). Across these previous measurements there is a significant spread in values depending on the methods used in calculating SFR ($\log(SFR/M_\odot\ yr^{-1}) = 1.29 - 1.49$ and $0.70 - 1.23$ for ID6355 and ID10612, respectively), indicating the assumptions involved play a non-trivial role in the final SFR estimates. As J. Brinchmann (2023), M. Curti et al. (2023), and S. Tacchella et al. (2023) estimate SFR from SED fitting, K. Nakajima et al. (2023) offer the best comparison to our results, as their estimated SFRs are also derived from dust-corrected Hβ fluxes. They measure $\log(SFR/M_\odot\ yr^{-1}) = 1.41 \pm 0.01$ and $1.14^{+0.01}_{-0.02}$ for ID6355 and ID10612, respectively. The SFR we derived for ID10612, $\log(SFR/M_\odot\ yr^{-1}) = 1.17 \pm 0.02$, is consistent with the K. Nakajima et al. (2023) within 2σ. In contrast, for ID6355, we find $\log(SFR/M_\odot\ yr^{-1}) = 1.73 \pm 0.03$ which is significantly higher than that measured by K. Nakajima et al. (2023), as the two values are not consistent within 3σ. We note K. Nakajima et al. (2023) have adopted the G. Chabrier (2003) IMF (initial mass function) in their SFR estimation, while we have applied SFR calibrations assuming a P. Kroupa & C. Weidner (2003) IMF, but R. C. Kennicutt & N. J. Evans (2012) comment that these IMFs should yield similar results. Hence, the discrepancy in measured SFR instead most likely arises because our integrated spectra are extracted from a larger area compared to the slit of the NIRSpec/MSA observations (see Fig. B1); hence, we obtain a more complete estimate of the total SFR of the galaxies using IFU spectra. This discrepancy is most significant for ID6355 as it is more extended than ID10612, and is therefore not as well covered by the MSA slit. Indeed, by comparing NIRSpec integrated spectra extracted from the MSA apertures to the galaxy-integrated spectra from Section 3.1, we estimate that the MSA

Downloaded from https://academic.oup.com/mnras/article/546/3/staag094/8426291 by guest on 31 March 2026

aperture misses up to 57 per cent and 15 per cent of the SFR in ID6355 and ID10612, respectively.

The difference in aperture size between the MSA and IFU could also drive discrepancies in measured ISM properties, particularly if key emission lines (e.g. [O III]λ4363) are poorly captured by the MSA slit. For instance, we now turn to electron temperature. Comparing to results from M. Curti et al. 2023, we first note that we have measured a consistent electron temperature for ID10612, finding $(1.8 \pm 0.4) \times 10^4$ K compared to their measurement of $(1.75 \pm 0.16) \times 10^4$ K. However, we find a significantly higher value for ID6355 compared to this earlier study (our value $(1.6 \pm 0.2) \times 10^4$ K compared to their value $(1.20 \pm 0.07) \times 10^4$ K). However, this analysis is based on the entire [O III]λλ4959, 5007 and Hβ line profiles. When recalculating T_e, now deconvolving the broad component detected in each galaxy, we instead find yet higher electron temperatures of $(1.8 \pm 0.4) \times 10^4$ and $(2.2 \pm 0.4) \times 10^4$ K, revealing discrepantly higher T_e for both galaxies, which naturally has implications for the direct-T_e metallicities we infer.

Compared to previous studies (K. Nakajima et al. 2023; M. Curti et al. 2023; S. Tacchella et al. 2023), our measured direct-T_e metallicities are significantly lower. In particular, in comparison to M. Curti et al. (2023), the direct-T_e metallicity we have identified for ID6355 ($7.90^{+0.30}_{-0.21}$) is significantly lower than their quoted value of 8.24 ± 0.07, but this value is consistent with ours to within 2σ. Furthermore, when recalculating the direct-T_e metallicity after removing the broad component, we measure values of $7.48^{+0.43}_{-0.27}$ and $7.12^{+0.24}_{-0.10}$ in ID6355 and ID10612, respectively; these values are significantly lower than our earlier estimate that included both narrow and broad components ($7.90^{+0.30}_{-0.21}$ and $7.70^{+0.22}_{-0.20}$), and discrepant to the values found by M. Curti et al. (2023), 8.24 ± 0.07 and 7.73 ± 0.12. This difference suggests the narrow and broad kinematical components in each galaxy have different metallicities and therefore distinct physical properties, which affects galaxy properties inferred from an overall line profile. Hence, when working with high-resolution spectra where separate broad components can be resolved, it is important to account for the presence of a broad component when making calculations of ISM properties.

Finally, Y. Xu et al. (2025) measure outflow properties in our target galaxies using the *R*1000 spectral data, finding a lower outflow velocity for ID6355 (386 ± 33 km s^{-1} compared to our value of 512^{+83}_{-84} km s^{-1}), but obtaining a comparable result for ID10612 (254 ± 35 km s^{-1} compared to 255^{+18}_{-27} km s^{-1}) within the respective errors. Furthermore, they have obtained mass-loading factors of 0.59 and 0.70 for ID6355 and ID10612, which are consistent with our measured values of $\eta = 0.3^{+0.3}_{-0.1}$ and $0.4^{+0.5}_{-0.2}$ within 1σ. With our IFS observations, we were able to directly estimate the outflow size, unlike MSA observation-based studies such as Y. Xu et al. (2025) which must rely on assumed sizes. Furthermore, the spatial resolution of our observations enabled us to trace outflows and SFRs more completely than would be possible with the MSA observations. These significant improvements of IFU over MSA, combined with the inherently uncertain nature of η, therefore do not allow for meaningful comparison between our results and those of Y. Xu et al. (2025).

6.2 Metallicity profile implications

Metallicity gradients bear the imprint of underlying processes such as gas accretion, SF, outflows, and mergers, as well as the interplay of these processes (R. Maiolino & F. Mannucci 2019). Overall, negative (radially decreasing) gradients are often interpreted as arising from inside–out galaxy formation, with stars forming earlier in the inner parts of a galaxy and having more time to chemically enrich the inner regions than the outer ones (A. M. Garcia et al. 2025b). Positive (radially increasing) gradients can be produced by accretion of external pristine gas towards the centre of the galaxy, or by metal-rich outflows from the galaxy centre driving metals outward (G. Cresci et al. 2010; P. Troncoso et al. 2014; J. Chisholm, C. Tremonti & C. Leitherer 2018). Flat gradients can arise from the radial mixing of gas or redistribution of metals on galaxy scales, as induced by SN winds or outflows (W. M. Baker et al. 2023); galaxy mergers can also produce flat gradients. Although we do not favour the merger scenario for the objects presented in this study (see Section 5.4), it is worth mentioning that, based on recent *JWST* observations, the galaxy major merger rate is $2 - 8$ Gyr^{-1} (D. Puskás et al. 2025). This is significantly higher than at low-z, meaning that it is likely that high-z galaxies have undergone one or more major mergers in their lifetimes, which will have had an impact on their observed metallicity profiles.

Studies of spatially resolved metallicity gradients are currently very limited at $z > 5$, and primarily present strong-line metallicity gradients. G. Venturi et al. (2024) measured metallicity gradients in a sample of three galaxies at $z \sim 6 - 8$, which are comparable to our targets in terms of their stellar mass and bulk gas-phase metallicity. They identify metallicity gradients of ~ -0.05 to $+0.14$ dex kpc^{-1}, flat within their uncertainties and consistent with processes mixing gas and metals on galaxy scales (i.e. mergers, outflows, or SN winds). L. Vallini et al. (2024) measure metallicity gradients in five UV-luminous Lyman-break galaxies at $z \sim 7$ to be mildly negative, also compatible with flat gradients within the uncertainties. R. Tripodi et al. (2024) infer slight positive gradients by analysing 2D slit spectra stacked along the slit; such inverted gradients could be tracing near-pristine gas inflows toward the centre; again, the gradients they measure are also consistent with being flat within the uncertainties. In contrast to these results, Z. Li et al. (2025) present an investigation of metallicity gradients around the redshift of our sources based on the stacking of grism spectra and find evidence of steep negative gradients, which they ascribe to inside-out growth with little feedback. They suggest that the flat gradients found by G. Venturi et al. (2024) might be due to the sample comprising of merging systems. However, we note that the stacking technique is subject to potential issues associated with combining galaxies with different sizes and properties. Finally, S. Arribas et al. (2024) have identified a gradient of ~ 0.1 dex kpc^{-1} across the whole structure of SPT0311-58-E, which they conclude is explained by accretion of pristine gas from the IGM. Overall, the flat gradients we measure in this study are therefore consistent with current observational picture of diverse metallicity gradients in the early Universe.

While the flat strong-line gradients and irregular metallicity distributions, we observe in our targets may be due to some merger activity (see Section 5.4), our favoured outflow scenario would suggest that that the negative gradients suggested by the analysis of Z. Li et al. (2025) are not ubiquitous among isolated galaxies at this cosmic epoch, and that metal redistribution via feedback processes might be at work in low-mass galaxies at these early times. A. M. Garcia et al. (2025a) also suggest that the flat gradients often measured at high-z may arise due to feedback

Downloaded from https://academic.oup.com/mnras/article/546/3/stag094/8426291 by guest on 31 March 2026

associated with bursty SF, though this association is less clear at the low-mass end.

In contrast to the strong-line results, the negative direct-T_e gradient inferred for ID6355 may point to inside–out structure formation and rotational support playing some role in its metallicity profile. The tension between our strong-line and direct-T_e results also highlights some of the challenges currently facing high-redshift metallicity gradient analyses. For example, the tension may arise in part due to strong-line calibrations being inappropriate for studying metallicity in the inner region of ID6355, as AGN ionization could artificially flatten the observed strong-line gradient. On the other hand, direct-T_e metallicity measurements assume a constant density applies to the aperture (e.g. Z. Martinez et al. 2025), which may not be a valid assumption in the case of clumpy high-z galaxies. A detailed study of how such factors affect measured strong-line and direct-T_e metallicity gradients, and of how to resolve this tension, is beyond the scope of this paper.

6.3 Comparison to outflow properties in local analogues and simulations

In Section 5.3, we argued that the broad component seen in the [O III]$\lambda\lambda$4959, 5007 emission line of ID6355 arises due to an outflow; we also suggested a tentative outflow detection in ID10612. In this section, we now discuss the impact of the detected outflows on their host galaxies.

The results from Sections 5.4 and 5.5 are consistent with findings at Cosmic Noon and local observations, which have shown the evidence for AGN feedback is subtle and elusive. Indeed, J. M. Piotrowska et al. (2022) and A. F. L. Bluck et al. (2022) have shown that the effect of AGN feedback is cumulative over many AGN episodes; hence, we do not expect to observe any strong evidence of AGN feedback on a short time-scale (J. Scholtz et al. 2020; I. Lamperti et al. 2021; J. Scholtz et al. 2024), so the low mass-loading factors calculated for our targets do not reveal the overall impact of the outflows. Furthermore, the lower velocities of our outflows are consistent with the findings of C. M. Harrison et al. (2016) and N. M. Förster Schreiber et al. (2019) of a strong correlation between outflow velocity and stellar mass, and also with the trend hinted at in Fig. 11 of outflow velocity decreasing toward earlier cosmic times in normal $M_* < 10^9$ M$_\odot$ AGN-host and SF galaxies. This evidence points towards slower outflows in early low-mass galaxies, increasing the difficulty of conclusively identifying outflows at high-z. A systematic, large-sample study accounting for both L_{bol} and M_* will be necessary to confirm this trend, but such an analysis is beyond the scope of this paper. Furthermore, both of our sources hosting redshifted outflow components indicates that outflow morphology may be complex or different to expectations at in the early Universe, further complicating the matter of identifying outflows.

In Fig. 12, we compare our detection of outflows in our high-z targets to the best local analogues we could identify in the literature: local AGN-host dwarf galaxies at $z < 1$ (from W. Liu et al. 2020; V. Rodríguez Morales et al. 2025). In terms of low mass-loading factor, our targets are consistent with some of these local dwarf galaxies; however, we note that although these dwarf galaxies are considered to be 'low-mass' *locally*, most of them have a stellar mass almost 0.5 dex higher than those of our targets. To properly evaluate how local dwarf galaxies compare to our high-redshift sample and investigate how AGN feedback evolves across cosmic time in low-mass systems, we would require a larger sample with lower mass local AGN-host dwarf galaxies. We also find that our observations are consistent with other *JWST*/NIRSpec samples from the literature, particularly those probing lower stellar mass (S. Carniani et al. 2024b), which ultimately show low mass-loading factors and $v_{out}/v_{esc} \sim 1$.

To assist with the further interpretation of our results, we make a comparison of our observations to the results of AESOPICA simulations. AESOPICA is a new suite of large-volume cosmological simulations (Koudmani et al., in preparation) built upon the FABLE galaxy formation model (N. A. Henden et al. 2018), with targeted updates for modelling the growth of infant SMBHs in the early Universe.AESOPICA explores three key modifications to fiducial galaxy formation models: enabling efficient accretion in the low-mass regime (S. Koudmani, D. Sijacki & M. C. Smith 2022), incorporating super-Eddington accretion, and examining a broad range of seed masses (10^2 to 10^5 M$_\odot$) following seed evolution from early cosmic epochs ($z \sim 20$). From the simulations, we select simulated AGN-host galaxies at $z \sim 7.6$, i.e. the redshift of our sources. The simulated galaxies roughly match the dynamical and stellar mass of our targets. We utilize three different simulation modes: (i) fiducial accretion following FABLE ('*Fiducial*'), (ii) boosted accretion allowing efficient AGN activity in low-mass galaxies following S. Koudmani et al. (2022) ('*BoostAcc*'), and (iii) boosted accretion with super-Eddington accretion (up to 10 times the Eddington limit; '*SuperEdd+BoostAcc*').

In the right-hand panel of Fig. 12, we note that outflows observed with *JWST* have a wide range of measured mass-loading factors scattered around $\eta \sim 1$. The results from the AESOPICA simulations on average have larger mass-loading factors, but display a considerable scatter at a fixed stellar mass with some simulated galaxies in good agreement with our observational estimates. We however caution that estimating the mass outflow rate in observations includes major systematic uncertainties with regards to the assumed density and metallicity of the outflow, resulting in systematic uncertainties of up to 1 dex (as discussed in Section 5.5). Furthermore, there are significant uncertainties in the modelling of high-redshift AGN in simulations and, crucially, in measuring the simulated outflow properties in an analogous manner to the observations (for a recent detailed discussion on this topic, see S. Martin-Alvarez et al. 2026). Importantly, the mass-weighted outflow velocities calculated from simulations are significantly biased low compared to outflow velocities inferred from mock observations based on the same simulations. We therefore utilize the 95th percentile of the (mass-weighted) gas velocity distribution as a more reliable tracer of the broad-line-based outflow velocity (see discussion in appendix B of S. Martin-Alvarez et al. 2026). Finally, we use Equation (10) to calculate the outflow rate, integrating over all outflowing mass between the observational resolution limit (conservatively ~ 40 km s^{-1}) and the outflow velocity based on the 95th percentile.

Although it is reassuring that the AESOPICA simulations contain some systems that resemble our observations (see Fig. 12), we ultimately cannot make any firm conclusions on the nature of the observed outflows. For a true apple-to-apple comparison, we would need to produce full mock observations of the AESOPICA outputs; however, this is beyond the scope of this exploratory work, and we defer utilizing this approach until future studies with larger samples of similar outflow observations. We stress that accounting for observational effects would likely increase the scatter in the simulated outflow distributions. Furthermore, outflows with low mass-loading factors and high outflow velocities

Downloaded from https://academic.oup.com/mnras/article/546/3/stag094/8426291 by guest on 31 March 2026

are more likely to arise from simulations with a resolved multi-phase ISM (see e.g. S. Koudmani et al. 2019; U. P. Steinwandel et al. 2022).

While we conclude the broad components in each galaxy correspond to outflows, we must also comment on what may be driving them. In simulations of dwarf galaxies without efficient AGN activity (our *Fiducial* model), the high outflow velocities observed for our targets are quite rare (see left-hand panel of Fig. 12). High outflow velocities are much more common in the AESOPICA simulations with boosted AGN accretion efficiency (i.e. the *BoostAcc* or *SuperEdd+BoostAcc* models). This is in line with previous results from the FABLE simulations (S. Koudmani et al. 2021) as well as high-resolution simulations of idealized galaxies (S. Koudmani et al. 2019). Interestingly, we found from our analysis of the simulations that high outflow velocities are generally associated with overmassive BHs (see Appendix D); this is also a common feature in AGN observed with *JWST* (e.g. H. Übler et al. 2023; R. Maiolino et al. 2024a; I. Juodžbalis et al. 2025). Combining with the tentative detection of an AGN in ID6355, we propose that this may be an example of an AGN-driven outflow operating in a low-mass galaxy in the early Universe. On the other hand, as we have not conclusively identified ID10612 as hosting an AGN, we cannot currently distinguish whether an outflow in this galaxy is driven by AGN or SF.

Our analysis of these galaxies has demonstrated that searching for outflows at the epoch of reionization is significantly more challenging than at lower redshifts. Low outflow velocities can result in outflows being confused with galactic rotation, merging galaxies or tidal interactions (A. Concas et al. 2022; G. C. Jones et al. 2025a; J. Scholtz et al. 2025c), requiring deep, high spectral resolution IFS observation to disentangle the different kinematical components.

7 CONCLUSIONS

In this work, we have presented a detailed analysis of new, high spectral resolution NIRSpec/IFS observations of two low-mass, potential AGN-host galaxies at $z \sim 7.6$. Through our integrated and spatially resolved investigations of the ISM properties and kinematics in our targets, we find that:

(i) Based on established AGN diagnostics based on the [O III]λ4363 auroral line, our observations of ID6355 are consistent with AGN ionization, while ID10612 is consistent with either AGN or SF activity (see Fig. 4). Combining with earlier results including the detection of high ionization lines ([Ne IV]$\lambda\lambda$2422, 2424; J. Brinchmann 2023) and full spectral fitting (M. S. Silcock et al. 2025), we conclude ID6355 hosts a Type-II AGN, while ID10612 remains a tentative AGN-host candidate.

(ii) Our results show marginal discrepancies in measured SFR and direct-T_e metallicity when compared to the results of earlier studies using the NIRSpec/MSA observations of these galaxies; we measure higher SFRs and lower metallicities overall, though almost all findings are consistent with earlier results within the associated uncertainties. The discrepancies can primarily be explained by difference in aperture size between the IFU and MSA observations.

(iii) Taking advantage of spatially resolved observations, we find evidence for flat strong-line metallicity gradients of -0.01 ± 0.01 and 0.00 ± 0.02 dex kpc^{-1} in ID6355 and ID10612 respectiely (Fig. 6). When compared to the limited previous studies of metallicity gradients in galaxies at comparable redshift (G. Venturi et al. 2024; L. Vallini et al. 2024; R. Tripodi et al. 2024; S. Arribas et al. 2024; Z. Li et al. 2025), our results suggest that a redistribution of metals is occurring on a galactic scale in our targets. We note that these gradients are not radially symmetric, and that while maps of strong-line metallicity (see Fig. 5) are not particularly reliable, they indicate the flat strong-line gradients may arise due to an irregular metallicity distribution in these galaxies.

(iv) We identify a negative direct-T_e metallicity gradient of -0.11 ± 0.03 dex kpc^{-1}, in significant tension with the strong-line result. This tension could arise from problems with the strong-line calibrations or the constant-density assumptions of the direct-T_e calculation. As we cannot distinguish between these scenarios without further study on these gradients in larger sample of galaxies, we conclude that ID6355 exhibits a flat-to-negative gradient, consistent with scenarios ranging from inside–out structure formation to gas mixing on kpc scales within the galaxy.

(v) Both galaxies exhibit complex kinematics with multiple components (see Section 5). ID6355 exhibits evidence for some rotational support with high dispersion (Fig. 7a), while ID10612 is completely dominated by dispersive motions (Fig. 7b). We identify v_{rot}/σ ratios of 0.63 ± 0.36 and < 0.36 in the respective galaxies, consistent with the emerging theoretical and observational picture of decreasing rotational support towards early cosmic times (Fig. 8).

(vi) By combining morphological modelling with our kinematics maps, we estimate intrinsic rotational velocities and constrain the dynamical masses of our targets. We find M_*/M_{dyn} ratios of 0.013 ± 0.010 and 0.015 ± 0.007 in ID6355 and ID10612, respectively, indicating high gas and/or dark matter fractions, consistent with findings for other early low-mass galaxies (e.g. A. Graaff et al. 2024).

(vii) We find strong evidence for an additional broad kinematical component in each galaxy, with FWHM $= 522 \pm 47$ and 275 ± 12 km s^{-1} in ID6355 and ID10612, respectively (Figs 9 and 10). We evaluate inflow, outflow, and merger scenarios as possible origins for this component, ultimately adopting the outflow interpretation in our analysis.

(viii) Assuming the broad component arises from an outflow in each galaxy, we constrain the associated outflow properties. We identify ionized outflows with v_{out} of 512^{+83}_{-84} and 255^{18}_{-27} km s^{-1}in ID6355 and ID10612, respectively, comparable to that measured for other high-redshift outflows (Fig. 11), but considerably lower than those associated with AGN at lower redshifts. We estimate outflow radii of ~ 1 kpc in each galaxy, indicating the outflows are spatially extended. We estimate mass outflow rates of 14^{+18}_{-6} and 8^{+11}_{-3} M$_\odot$ yr^{-1} in ID6355 and ID10612, respectively. Both galaxies have mass-loading factors $\eta < 1$ (see the right-hand panel of Fig. 12), illustrating that at this point in cosmic time, the outflows cannot completely quench SF in their galaxies. However, we additionally estimate the escape velocity of each galaxy based on estimated dynamical masses, finding that the measured outflows are capable of driving gas out of the galaxies into the CGM (see the left-hand panel of Fig. 12) and could contribute to the suppression of SF over longer time-scales. We also show that the outflow properties of our systems and of high-z AGN observed with *JWST* are consistent within systematic uncertainties.

(ix) To investigate the outflow origins, we compare the outflow properties of our targets with those from the new AESOPICA simulations (Koudmani et al., in preparation) of $z \sim 7.6$ AGN-host dwarf galaxies in Section 6.3 and Fig. 12. We find v_{out}/v_{esc} ratios that are more commonly associated with the simulations includ-

Downloaded from https://academic.oup.com/mnras/article/546/3/stag094/8426291 by guest on 31 March 2026

ing efficient AGN accretion at early cosmic times. We also find that our measured mass-loading factors can be reproduced by simulated systems of similar stellar and dynamical mass. These observations together hint that AGN activity could be the driver of the detected outflows. However, we caution that the majority of simulated galaxies have larger η values, and stress that η is a largely uncertain outflow parameter across both simulations and observations. Mock observations, when combined with a larger future observational sample, will be necessary to tackle the larger issue of cosmological simulations tending to find larger mass-loading factors than observations. Hence, we cannot conclusively state whether the measured outflows are driven by AGN or by SF.

Overall, this novel study demonstrates the importance of obtaining deep NIRSpec/IFS observations of low-mass galaxies at $z > 7$, as such observations enable detailed, spatially resolved analyses of the galaxy properties and kinematics in this challenging, poorly understood demographic. The high spatial-resolution observations possible with NIRSpec/IFS are particularly crucial for disentangling any detected broad components from galactic rotation, and for evaluating the origin of these broad components. The galaxies discussed in this work represent just a small fraction of a wider high-z population of low-mass galaxies within which AGN feedback may be operating. Future spatially resolved studies based on deep NIRSpec/IFU observations, similar to that presented in this work, will therefore be crucial to our wider understanding of how outflows influence the kinematics, chemical enrichment, and overall evolution of low-mass galaxies at this epoch.

ACKNOWLEDGEMENTS

We thank the anonymous referee for their thoughtful comments, which helped improve the quality of this paper. We thank Giovanni Mazzolari for providing the base code and data compilation for AGN diagnostic diagrams shown in this work.

LRI, JS, GCJ, FDE, and RM acknowledge support by the Science and Technology Facilities Council (STFC), ERC advanced grant 695671 'QUENCH' and the UKRI Frontier Research grant RISEandFALL. ALD thanks the University of Cambridge Harding Distinguished Postgraduate Scholars Programme and Technology Facilities Council (STFC) Center for Doctoral Training (CDT) in Data Intensive Science at the University of Cambridge (STFC grant no. 2742605) for a PhD studentship, and gratefully acknowledges support by the Royal Society Research Grant G125142. SK has been supported by a Junior Research Fellowship from St Catharine's College, Cambridge and a Research Fellowship from the Royal Commission for the Exhibition of 1851. RM also acknowledges funding from a research professorship from the Royal Society. MC acknowledges support from ESO via the ESO Fellowship Europe. ST acknowledges support by the Royal Society Research Grant G125142. WMB gratefully acknowledges support from DARK via the DARK fellowship. This work was supported by a research grant (VIL54489) from VILLUM FONDEN. SA acknowledges grant PID2021-127718NB-I00 funded by the Spanish Ministry of Science and Innovation/State Agency of Research (MICIN/AEI/ 10.13039/501100011033). DJE is supported as a Simons Investigator and by *JWST*/NIRCam contract to the University of Arizona, NAS5-02015 and by NASA through a grant from the Space Telescope Science Institute, which is operated by the Association of Universities for Research in Astronomy, Inc., under NASA contract NAS 5–03127. ZJ acknowledges *JWST*/NIRCam contract to the University of Arizona, NAS5-02015. MK thanks the University of Cambridge Harding Distinguished Postgraduate Scholars Programme, UK STFC CDT in Data Intensive Science, and Girton College Cambridge for a PhD studentship. MP acknowledges support through the grants PID2021-127718NB-I00 and RYC2023-044853-I, funded by the Spain Ministry of Science and Innovation/State Agency of Research MCIN/AEI/10.13039/501100011033 and El Fondo Social Europeo Plus FSE+. DP acknowledges support by the Huo Family Foundation through a P.C. Ho PhD Studentship. BER acknowledges support from the NIRCam Science Team contract to the University of Arizona, NAS5-02015, and *JWST* program 3215. DS acknowledges support from the STFC, grant code ST/W000997/1. JAAT acknowledges support from the Simons Foundation and *JWST* program 3215. Support for program 3215 was provided by NASA through a grant from the Space Telescope Science Institute, which is operated by the Association of Universities for Research in Astronomy, Inc., under NASA contract NAS 5–03127. CW acknowledges support from the Swiss State Secretariat for Education, Research and Innovation (SERI) under contract no. MB22.00072.

This work is based on observations made with the NASA/ESA/CSA *James Webb Space Telescope*. The data were obtained from the Mikulski Archive for Space Telescopes (MAST) at the Space Telescope Science Institute, which is operated by the Association of Universities for Research in Astronomy, Inc., under NASA contract NAS 5–03127 for *JWST*. These observations are associated with *JWST* program IDs 2736 and 2959.

DATA AVAILABILITY

We use publicly available *JWST*/NIRSpec and NIRCam data, which can be downloaded from the MAST (https://mast.stsci.edu/portal/Mashup/Clients/Mast/Portal.html) under PIDs 2959 and 2736, respectively.

REFERENCES

Acharyya A. et al., 2025, preprint (arXiv:2508.05335)
Allen N. et al., 2025, A&A, 698, A30
Amorín R. et al., 2015, A&A, 578, A105
Arjona-Gálvez E., Di Cintio A., Grand R. J. J., 2024, A&A, 690, A286
Arrabal Haro P. et al., 2023, Nature, 622, 707
Arribas S. et al., 2024, A&A, 688, A146
Asplund M., Grevesse N., Sauval A. J., Scott P., 2009, ARA&A, 47, 481
Baker W. M. et al., 2023, MNRAS, 519, 1149
Baker W. M. et al., 2025a, MNRAS, 539, 557
Baker W. M. et al., 2025b, A&A, 697, A90
Baker W. M. et al., 2025c, A&A, 702, A270
Bennett J. S., Sijacki D., Costa T., Laporte N., Witten C., 2024, MNRAS, 527, 1033
Berg D. A. et al., 2012, ApJ, 754, 98
Bertola E. et al., 2025, A&A, 699, A220
Bezanson R. et al., 2018, ApJ, 868, L36
Bischetti M. et al., 2017, A&A, 598, A122
Bischetti M. et al., 2024, ApJ, 970, 9
Bluck A. F. L., Maiolino R., Brownson S., Conselice C. J., Ellison S. L., Piotrowska J. M., Thorp M. D., 2022, A&A, 659, A160
Böker T. et al., 2022, A&A, 661, A82
Brazzini M., D'Odorico V., Bischetti M., Feruglio C., Cupani G., Becker G., Tripodi R., 2025, A&A, 698, A145
Brinchmann J., 2023, MNRAS, 525, 2087
Brownson S., Maiolino R., Tazzari M., Carniani S., Henden N., 2019, MNRAS, 490, 5134

Downloaded from https://academic.oup.com/mnras/article/546/3/stag094/8426291 by guest on 31 March 2026

Calzetti D., Armus L., Bohlin R. C., Kinney A. L., Koornneef J., Storchi-Bergmann T., 2000, ApJ, 533, 682
Calzetti D., Kinney A. L., Storchi-Bergmann T., 1994, ApJ, 429, 582
Cameron A. J. et al., 2023, A&A, 677, A115
Caminha G. B., Suyu S. H., Mercurio A., Brammer G., Bergamini P., Acebron A., Vanzella E., 2022, A&A, 666, L9
Cappellari M. et al., 2006, MNRAS, 366, 1126
Carnall A. C. et al., 2023a, MNRAS, 518, L45
Carnall A. C. et al., 2023b, MNRAS, 520, 3974
Carnall A. C. et al., 2023c, Nature, 619, 716
Carniani S. et al., 2015, A&A, 580, A102
Carniani S. et al., 2024a, Nature, 633, 318
Carniani S. et al., 2024b, A&A, 685, A99
Carniani S. et al., 2025, A&A, 696, A87
Castellano M. et al., 2024, ApJ, 972, 143
Cataldi E. et al., 2025, A&A, 703, A208
Chabrier G., 2003, PASP, 115, 763
Chisholm J., Tremonti C., Leitherer C., 2018, MNRAS, 481, 1690
Concas A. et al., 2022, MNRAS, 513, 2535
Cooper R. A., Caputi K. I., Iani E., Rinaldi P., Desprez G., Navarro-Carrera R., 2025, ApJ, 994, 102
Covelo-Paz A. et al. 2026, A&A, 705, A155
Cresci G. et al., 2023, A&A, 672, A128
Cresci G., Mannucci F., Maiolino R., Marconi A., Gnerucci A., Magrini L., 2010, Nature, 467, 811
Curti M., Cresci G., Mannucci F., Marconi A., Maiolino R., Esposito S., 2017, MNRAS, 465, 1384
Curti M. et al., 2020b, MNRAS, 492, 821
Curti M. et al., 2023, MNRAS, 518, 425
Curti M. et al., 2024, A&A, 684, A75
Curti M., Mannucci F., Cresci G., Maiolino R., 2020a, MNRAS, 491, 944
Curtis-Lake E. et al., 2023, Nat. Astron., 7, 622
D'Eugenio F. et al., 2024a, Nat. Astron., 8, 1443
D'Eugenio F. et al., 2024b, A&A, 689, A152
D'Eugenio F. et al., 2026, MNRAS, 545, staf2117
Danhaive A. L. et al., 2025, MNRAS, 543, 3249
Danhaive A. L. et al. 2026, MNRAS,
Davies R. L. et al., 2020, ApJ, 894, 28
de Graaff A. et al., 2024, A&A, 684, A87
Dekel A., Burkert A., 2014, MNRAS, 438, 1870
Dimitrijević M. S., Popović L. Č., Kovačević J., Dačić M., Ilić D., 2007, MNRAS, 374, 1181
Dome T., Martin-Alvarez S., Tacchella S., Yuan Y., Sijacki D., 2025, MNRAS, 537, 629
Dome T., Tacchella S., Fialkov A., Ceverino D., Dekel A., Ginzburg O., Lapiner S., Looser T. J., 2024, MNRAS, 527, 2139
Domínguez A. et al., 2013, ApJ, 763, 145
Donnan C. T. et al., 2025, ApJ, 993, 224
Dors O. L., Maiolino R., Cardaci M. V., Hägele G. F., Krabbe A. C., Pérez-Montero E., Armah M., 2020, MNRAS, 496, 3209
Dressler A. et al., 2024, ApJ, 964, 150
Du P., Wang J.-M., Hu C., Valls-Gabaud D., Baldwin J. A., Ge J.-Q., Xue S.-J., 2014, MNRAS, 438, 2828
El-Badry K., Wetzel A., Geha M., Hopkins P. F., Kereš D., Chan T. K., Faucher-Giguère C.-A., 2016, ApJ, 820, 131
Endsley R., Stark D. P., Whitler L., Topping M. W., Chen Z., Plat A., Chisholm J., Charlot S., 2023, MNRAS, 524, 2312
Feltre A., Charlot S., Gutkin J., 2016, MNRAS, 456, 3354
Fiore F. et al., 2017, A&A, 601, A143
Förster Schreiber N. M. et al., 2018, ApJS, 238, 21
Förster Schreiber N. M. et al., 2019, ApJ, 875, 21
Förster Schreiber N. M., Wuyts S., 2020, ARA&A, 58, 661
Fujimoto S. et al., 2025, preprint (arXiv:2510.16116)
Furtak L. J. et al., 2024, Nature, 628, 57
Garcia A. M. et al., 2025a, preprint (arXiv:2510.26877)
Garcia A. M. et al., 2025b, ApJ, 989, 147
Gelli V., Salvadori S., Ferrara A., Pallottini A., 2024, ApJ, 964, 76
Girard M. et al., 2021, ApJ, 909, 12
Glazebrook K. et al., 2024, Nature, 628, 277
González-Alfonso E. et al., 2017, ApJ, 836, 11
Greene J. E. et al., 2024, ApJ, 964, 39
Groves B., Brinchmann J., Walcher C. J., 2012, MNRAS, 419, 1402
Harikane Y. et al., 2023, ApJ, 959, 39
Harrison C. M. et al., 2016, MNRAS, 456, 1195
Hemler Z. S. et al., 2021, MNRAS, 506, 3024
Henden N. A., Puchwein E., Shen S., Sijacki D., 2018, MNRAS, 479, 5385
Herrera-Camus R. et al., 2025, A&A, 699, A80
Hopkins P. F. et al., 2023, MNRAS, 525, 2241
Hsiao T. Y.-Y. et al., 2023, ApJ, 949, L34
Hsiao T. Y.-Y. et al., 2025, preprint (arXiv:2505.03873)
Isobe Y., Ouchi M., Nakajima K., Harikane Y., Ono Y., Xu Y., Zhang Y., Umeda H., 2023, ApJ, 956, 139
Izotov Y. I., Guseva N. G., Fricke K. J., Henkel C., 2019, A&A, 623, A40
Izotov Y. I., Stasińska G., Meynet G., Guseva N. G., Thuan T. X., 2006, A&A, 448, 955
Izotov Y. I., Thuan T. X., 2007, ApJ, 665, 1115
Izotov Y. I., Thuan T. X., Guseva N. G., Liss S. E., 2018, MNRAS, 473, 1956
Jakobsen P. et al., 2022, A&A, 661, A80
Ji X. et al., 2024, MNRAS, 535, 881
Ji Z. et al., 2024, preprint (arXiv:2401.00934)
Johnson B. D., 2019, Astrophysics Source Code Library, record ascl:1905.026
Jones G. C. et al., 2024a, preprint (arXiv:2412.15027)
Jones G. C. et al., 2024b, A&A, 682, A122
Jones G. C. et al., 2025a, MNRAS, 540, 3311
Jones G. C. et al., 2025b,preprint (arXiv:2509.20455)
Jones G. C., Maiolino R., Carniani S., Circosta C., Fudamoto Y., Scholtz J., 2023, MNRAS, 522, 275
Juodžbalis I. et al., 2024, Nature, 636, 594
Juodžbalis I. et al., 2025, preprint (arXiv:2504.03551)
Kakkad D. et al., 2020, A&A, 642, A147
Kartaltepe J. S. et al., 2023, ApJ, 946, L15
Kennicutt R. C., Evans N. J., 2012, ARA&A, 50, 531
Kennicutt R. C. , Jr, 1998, ApJ, 498, 541
Kewley L. J., Nicholls D. C., Sutherland R. S., 2019, ARA&A, 57, 511
Kocevski D. D. et al., 2023, ApJ, 954, L4
Kohandel M., Pallottini A., Ferrara A., Zanella A., Rizzo F., Carniani S., 2024, A&A, 685, A72
Kokorev V. et al., 2023, ApJ, 957, L7
Koudmani S., Henden N. A., Sijacki D., 2021, MNRAS, 503, 3568
Koudmani S., Sijacki D., Bourne M. A., Smith M. C., 2019, MNRAS, 484, 2047
Koudmani S., Sijacki D., Smith M. C., 2022, MNRAS, 516, 2112
Kroupa P., Weidner C., 2003, ApJ, 598, 1076
Kumari N., Maiolino R., Trussler J., Mannucci F., Cresci G., Curti M., Marconi A., Belfiore F., 2021, A&A, 656, A140
Lamastra A., Bianchi S., Matt G., Perola G. C., Barcons X., Carrera F. J., 2009, A&A, 504, 73
Lamperti I. et al., 2021, A&A, 654, A90
Lamperti I. et al., 2024, A&A, 691, A153
Langeroodi D. et al., 2023, ApJ, 957, 39
Langeroodi D., Hjorth J., 2024, preprint (arXiv:2404.13045)
Laporte N., Zitrin A., Dole H., Roberts-Borsani G., Furtak L. J., Witten C., 2022, A&A, 667, L3
Laseter I. H. et al., 2024, A&A, 681, A70
Le Fèvre O. et al., 2020, A&A, 643, A1
Lelli F., Di Teodoro E. M., Fraternali F., Man A. W. S., Zhang Z.-Y., De Breuck C., Davis T. A., Maiolino R., 2021, Science, 371, 713
Liu W., Veilleux S., Canalizo G., Rupke D. S. N., Manzano-King C. M., Bohn T., U V., 2020, ApJ, 905, 166
Li Z. et al., 2023, preprint (arXiv:2310.09327)
Li Z. et al., 2025, ApJS, 280, 62
Looser T. J. et al., 2024, Nature, 629, 53
Looser T. J. et al., 2025, A&A, 697, A88
Luridiana V., Morisset C., Shaw R. A., 2015, A&A, 573, A42
Lutz D. et al., 2020, A&A, 633, A134

Downloaded from https://academic.oup.com/mnras/article/546/3/stag094/8426291 by guest on 31 March 2026

Mahler G. et al., 2023, ApJ, 945, 49
Maiolino R. et al., 2012, MNRAS, 425, L66
Maiolino R. et al., 2024a, Nature, 627, 59
Maiolino R. et al., 2024b, A&A, 691, A145
Maiolino R. et al., 2025a, preprint (arXiv:2505.22567)
Maiolino R. et al., 2025b, MNRAS, 538, 1921
Maiolino R., Mannucci F., 2019, A&AR, 27, 3
Marcelin L. C., Champagne J. B., Wang F., Fan X., Pudoka M., Tee W. L., Zhu Y., 2025, Res. Notes Am. Astron. Soc., 9, 133
Marconcini C. et al., 2024, MNRAS, 533, 2488
Marshall M. A. et al., 2023, A&A, 678, A191
Marshall M. A. et al., 2025, A&A, 702, A50
Martin-Alvarez S. et al., 2026, MNRAS, 545, staf2106
Martinez Z. et al., 2025, ApJ, 995, 204
Matthee J. et al., 2024, ApJ, 963, 129
Mazzolari G. et al., 2024a, preprint (arXiv:2412.04224)
Mazzolari G. et al., 2024b, A&A, 691, A345
Mazzolari G. et al., 2025, A&A, 700, A12
McClymont W. et al., 2025a, MNRAS, 540, 190
McClymont W. et al., 2025b, MNRAS, 544, 513
McClymont W. et al., 2025c, MNRAS, 544, 1732
Miller T. B. et al., 2025, ApJ, 988, 196
Morishita T. et al., 2024, ApJ, 963, 9
Naidu R. P. et al., 2025, preprint (arXiv:2505.11263)
Nakajima K. et al., 2022, ApJS, 262, 3
Nakajima K. et al., 2025, preprint (arXiv:2506.11846)
Nakajima K., Maiolino R., 2022, MNRAS, 513, 5134
Nakajima K., Ouchi M., Isobe Y., Harikane Y., Zhang Y., Ono Y., Umeda H., Oguri M., 2023, ApJS, 269, 33
Nanayakkara T. et al., 2024, Sci. Rep., 14, 3724
Nanayakkara T. et al., 2025, ApJ, 981, 78
Netzer H., 2009, MNRAS, 399, 1907
Onoue M. et al., 2023, ApJ, 942, L17
Osterbrock D. E., 1989, Astrophysics of Gaseous Nebulae and Active Galactic Nuclei. University Science Books, CA, USA
Osterbrock D. E., Ferland G. J., 2006, Astrophysics of Gaseous Nebulae and Active Galactic Nuclei. University Science Books, CA, USA
Parlanti E., Carniani S., Pallottini A., Cignoni M., Cresci G., Kohandel M., Mannucci F., Marconi A., 2023, A&A, 673, A153
Parlanti E. et al., 2024, A&A, 684, A24
Parlanti E. et al., 2025, A&A, 695, A6
Pascale M. et al., 2022, ApJ, 938, L6
Pasha I., Miller T. B., 2023, J. Open Source Softw., 8, 5703
Pérez-González P. G. et al., 2025, Nat. Astron., 9, 1240
Perna M., Cresci G., Brusa M., Lanzuisi G., Concas A., Mainieri V., Mannucci F., Marconi A., 2019, A&A, 623, A171
Perna M. et al., 2023, A&A, 679, A89
Perna M. et al., 2025, A&A, 694, A170
Pillepich A. et al., 2019, MNRAS, 490, 3196
Piotrowska J. M., Bluck A. F. L., Maiolino R., Peng Y., 2022, MNRAS, 512, 1052
Pontoppidan K. M. et al., 2022, ApJ, 936, L14
Price S. H. et al., 2020, ApJ, 894, 91
Puskás D. et al., 2025, MNRAS, 540, 2146
Pustilnik S. A., Egorova E. S., Kniazev A. Y., Perepelitsyna Y. A., Tepliakova A. L., Burenkov A. N., Oparin D. V., 2021, MNRAS, 507, 944
Pustilnik S. A., Kniazev A. Y., Perepelitsyna Y. A., Egorova E. S., 2020, MNRAS, 493, 830
Qiu Y., McNamara B. R., Bogdanović T., Inayoshi K., Ho L. C., 2021, ApJ, 923, 256
Reddy N. A., Topping M. W., Sanders R. L., Shapley A. E., Brammer G., 2023, ApJ, 952, 167
Rizzo F. et al., 2024, A&A, 689, A273
Rizzo F., Vegetti S., Powell D., Fraternali F., McKean J. P., Stacey H. R., White S. D. M., 2020, Nature, 584, 201
Robertson B. et al., 2024, ApJ, 970, 31
Rodríguez Del Pino B. et al., 2024, A&A, 684, A187
Rodríguez Morales V., Mezcua M., Domínguez Sánchez H., Audibert A., Müller-Sánchez F., Siudek M., Eróstegui A., 2025, A&A, 697, A235
Rowland L. E. et al., 2024, MNRAS, 535, 2068
Rupke D. S., Veilleux S., Sanders D. B., 2005, ApJS, 160, 115
Sanders R. L. et al., 2015, ApJ, 799, 138
Sanders R. L., Shapley A. E., Topping M. W., Reddy N. A., Brammer G. B., 2023, ApJ, 955, 54
Schaerer D., Marques-Chaves R., Barrufet L., Oesch P., Izotov Y. I., Naidu R., Guseva N. G., Brammer G., 2022, A&A, 665, L4
Scholtz J. et al., 2020, MNRAS, 492, 3194
Scholtz J. et al., 2024, preprint (arXiv:2405.19401)
Scholtz J. et al., 2025a, MNRAS, 544, L113
Scholtz J. et al., 2025b, preprint (arXiv:2510.01034)
Scholtz J. et al., 2025c, MNRAS, 539, 2463
Scholtz J. et al., 2025d, A&A, 697, A175
Sharma R. S., Brooks A. M., Tremmel M., Bellovary J., Quinn T. R., 2023, ApJ, 957, 16
Shivaei I. et al., 2020, ApJ, 899, 117
Silcock M. S. et al., 2025, MNRAS, 541, 3822
Simons R. C. et al., 2021, ApJ, 923, 203
Steinwandel U. P., Dolag K., Lesch H., Burkert A., 2022, ApJ, 924, 26
Strait V. et al., 2023, ApJ, 949, L23
Swinbank A. M., Sobral D., Smail I., Geach J. E., Best P. N., McCarthy I. G., Crain R. A., Theuns T., 2012, MNRAS, 426, 935
Tacchella S., Dekel A., Carollo C. M., Ceverino D., DeGraf C., Lapiner S., Mandelker N., Primack J. R., 2016, MNRAS, 458, 242
Tacchella S. et al., 2023, MNRAS, 522, 6236
Tacchella S. et al., 2025, MNRAS, 540, 851
Taylor A. J. et al., 2025, ApJ, 989, L7
Theios R. L., Steidel C. C., Strom A. L., Rudie G. C., Trainor R. F., Reddy N. A., 2019, ApJ, 871, 128
Topping M. W. et al., 2024, MNRAS, 529, 3301
Tozzi G. et al., 2024, A&A, 690, A141
Treu T. et al., 2023, ApJ, 942, L28
Tripodi R. et al., 2024, A&A, 692, A184
Troncoso P. et al., 2014, A&A, 563, A58
Trump J. R. et al., 2023, ApJ, 945, 35
Tully R. B., Pierce M. J., Huang J.-S., Saunders W., Verheijen M. A. W., Witchalls P. L., 1998, AJ, 115, 2264
Turner C. et al., 2025, MNRAS, 537, 1826
Übler H. et al., 2019, ApJ, 880, 48
Übler H. et al., 2023, A&A, 677, A145
Übler H. et al., 2024, MNRAS, 531, 355
Vallini L. et al., 2024, MNRAS, 527, 10
van der Wel A. et al., 2014, ApJ, 792, L6
van der Wel A. et al., 2022, ApJ, 936, 9
van Dokkum P. G., 2001, PASP, 113, 1420
Vanzella E. et al., 2023, A&A, 678, A173
Vayner A. et al., 2025, ApJ, 989, 230
Venturi G. et al., 2024, A&A, 691, A19
Wang X. et al., 2017, ApJ, 837, 89
Wang X. et al., 2022, ApJ, 938, L16
Weibel A. et al., 2024, MNRAS, 533, 1808
Weibel A. et al., 2025, ApJ, 983, 11
Westcott L. et al., 2025, ApJ, 983, 121
Wisnioski E. et al., 2015, ApJ, 799, 209
Witten C. et al., 2025a, preprint (arXiv:2507.06284)
Witten C. et al., 2025c, MNRAS, 537, 112
Witten C., Oesch P. A., Bennett J. S., Meyer R. A., Giovinazzo E., Covelo-Paz A., Baker W. M., Ivey L. R., 2025b, preprint (arXiv:2511.05647)
Wuyts E. et al., 2016, ApJ, 827, 74
Xu Y., Ouchi M., Nakajima K., Harikane Y., Isobe Y., Ono Y., Umeda H., Zhang Y., 2025, ApJ, 984, 182
Zamora S. et al., 2025, A&A, 702, A102
Zhang Y., Ouchi M., Nakajima K., Harikane Y., Isobe Y., Xu Y., Ono Y., Umeda H., 2024, ApJ, 970, 19
Zhu Y. et al., 2025, preprint (arXiv:2504.02305)

Downloaded from https://academic.oup.com/mnras/article/546/3/stag094/8426291 by guest on 31 March 2026

APPENDIX A: PSF DETERMINATION

In this work, we derive the instrumental PSF of the NIRSpec/IFU (shown, for example, in Figs 2, 3, and 7(a) and (b) based on a point source present in the FoV of our observation of ID6355 (see Fig. A1). The PSF corresponding to a particular emission line is calculated by fitting an image of the IFU cube, collapsed over a narrow-wavelength range centred on that line, with a 2D Gaussian (see Fig. A2). Noting that the observations of ID6355 and ID10612 were taken with only a short interval of time between them, we assume that same PSFs applied to our observations of ID10612. This star was also used as a test of our astrometry realignment (described in Section 2.4).

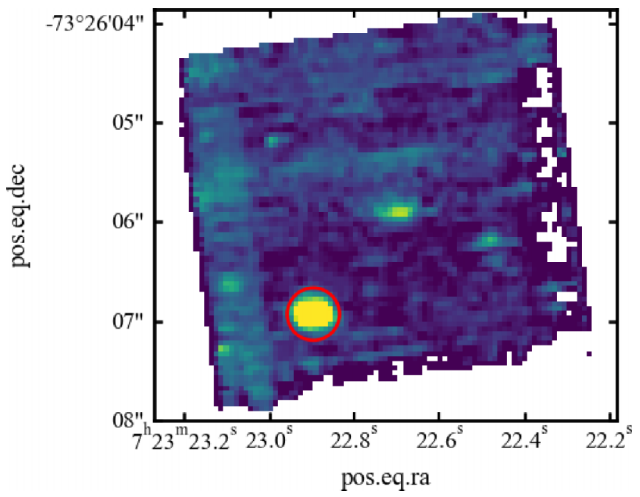

Figure A1. Mock *F*356*W* NIRCam image created from the NIRSpec/IFU observation of ID6355, showing the full IFU FoV. The point source present in the FoV used for PSF determination is shown circled in red. The large blob of emission at the centre of the figure corresponds to ID6355. The IFU data shown here have been realigned to match the NIRCam observations.

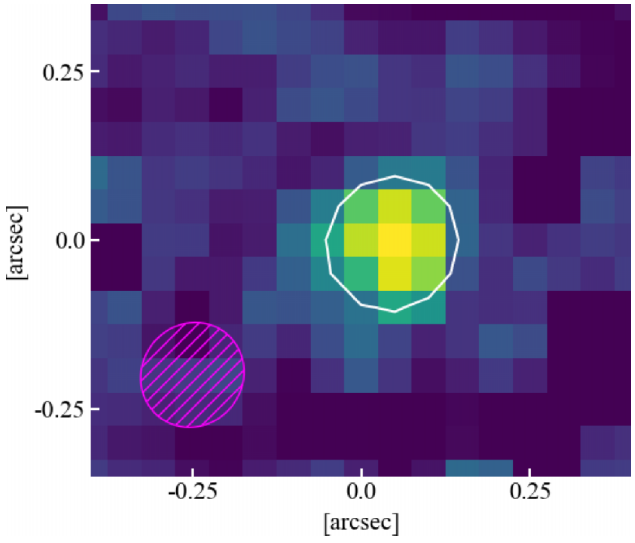

Figure A2. Image of the star visible in the FoV of the ID6355 observation, collapsed over the [O III]λ5007 emission line. The image is fitted with a 2D Gaussian to calculate the associated PSF, with a white contour plotted at the 1σ confidence interval. The magenta hatched ellipse in the bottom left illustrates the fitted PSF for comparison.

APPENDIX B: MSA AND IFU APERTURE COMPARISON

As discussed in Section 6.1, we compare our results to earlier results obtained from the MSA observations. In Fig. B1, we highlight the difference in aperture size between the IFU and MSA observations of our targets. This illustrates that the 0.25 arcsec radius apertures chosen to derive integrated galaxy properties from IFU data capture the bulk of each galaxy's [O III]λλ4959, 5007 flux, including galaxy regions not captured by the MSA observations. Furthermore, the 0.5 and 0.4 arcsec radius apertures fully capture any SF in ID6355 and ID10612, respectively, offering a far

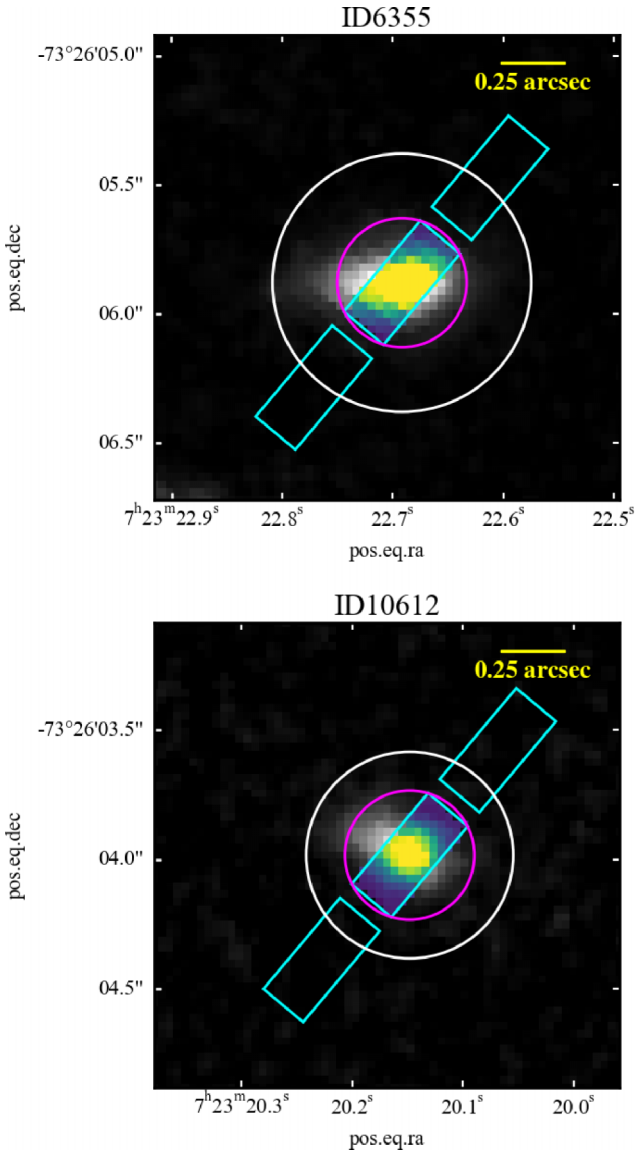

Figure B1. NIRCam *F*444*W* cutouts of each galaxy (top panel: ID6355 and bottom panel: ID10612), illustrating the sizes of the MSA and IFU apertures. The MSA apertures are shown as the cyan rectangles, with each central rectangle showing while the region of galaxy flux extraction while the surrounding two rectangles show the background detections. The IFU apertures used to calculate galaxy-integrated properties in this study, circular apertures of radius 0.25 arcsec for both galaxies, are shown in magenta. The IFU apertures used to calculate overall SFRs, of radii 0.5 arcsec (ID6355) and 0.4 arcsec (ID10612), are shown in white.

Downloaded from https://academic.oup.com/mnras/article/546/3/stag094/8426291 by guest on 31 March 2026

more complete picture of the total SFR than provided by the MSA observations.

APPENDIX C: PYSERSIC FITTING

As briefly introduced in Section 3.3, we model the *F*444*W* NIRCam images of our two galaxies using a Sérsic profile in order to estimate parameters, such as the inclination, which are needed to de-project and interpret the measured kinematics. This modelling also adds insight into the morphology of the two systems. We use the Bayesian code PySersic with a one-component model, and additionally fit a for a flat sky background, using the relevant NIRCam *F*444*W* PSF, derived following the methodology of Z. Ji et al. (2024). This is done to ensure that any residual background flux does not bias the modelling of the source itself. No masking is needed, as there as there are no neighbouring sources in the cutouts. The results are shown in Figs C1 and C2. As seen in the residuals, the single Sérsic model does not reproduce the

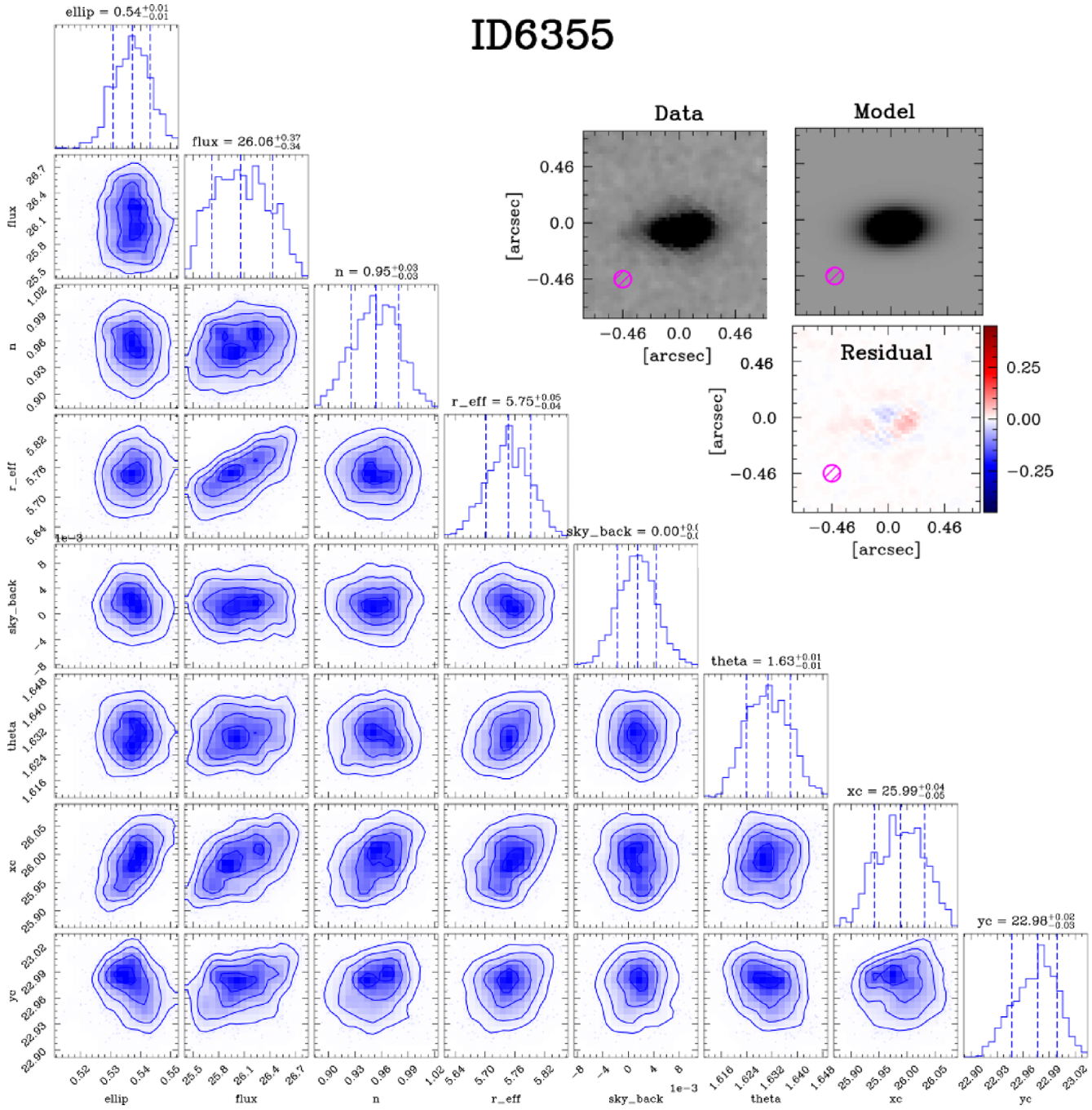

Figure C1. A visual summary of results from fitting ID6355 with PySersic. The bottom left of the figure shows the posterior distributions of the fitted parameters, along with best-fitting values with their associated errors. The top-right corner contains the data, model, and residual plots. The magenta hatched ellipse in each of the model/data/residual plots shows the NIRCam PSF.

Downloaded from https://academic.oup.com/mnras/article/546/3/stag094/8426291 by guest on 31 March 2026

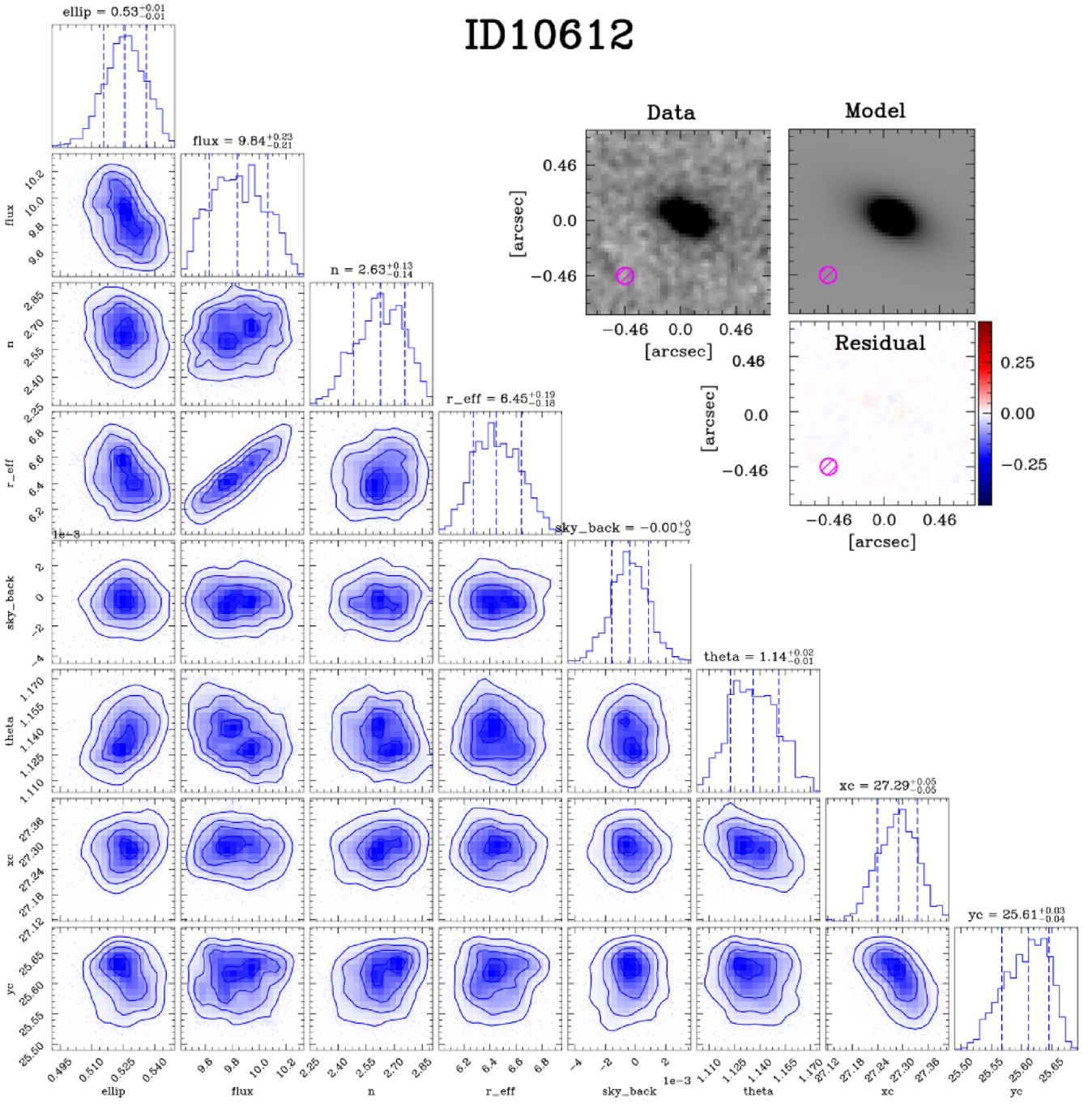

Figure C2. A visual summary of results from fitting ID10612 with PySersic. The bottom left of the figure shows the posterior distributions of the fitted parameters, along with the best-fitting values and their associated errors. The top-right corner contains the data, model, and residual plots. The magenta hatched ellipse in each of the model/data/residual plots shows the NIRCam PSF.

entire light profile, which is expected in galaxies at high redshift which are in earlier stages of their assembly history and hence tend to be clumpier. However, the fits remain satisfactory and are representative of the galaxy size and inclination.

APPENDIX D: RESULTS FROM SIMULATIONS

As discussed in Section 6.3, we compare our results to three variations within the AESOPICA simulation suite (*Fiducial*, *BoostAcc*, and *SuperEdd+BoostAcc*). In Fig. D1, we summarize the simulated outflow properties of each variant as functions of stellar mass. Across all three variations (but most notably for the models with boosted AGN accretion), for a given stellar mass, higher outflow velocities, and mass-loading factors appear to be associated with overmassive black holes ($M_{\rm BH} \sim 10^6$ M$_\odot$ for our stellar mass range of interest).

Downloaded from https://academic.oup.com/mnras/article/546/3/stag094/8426291 by guest on 31 March 2026

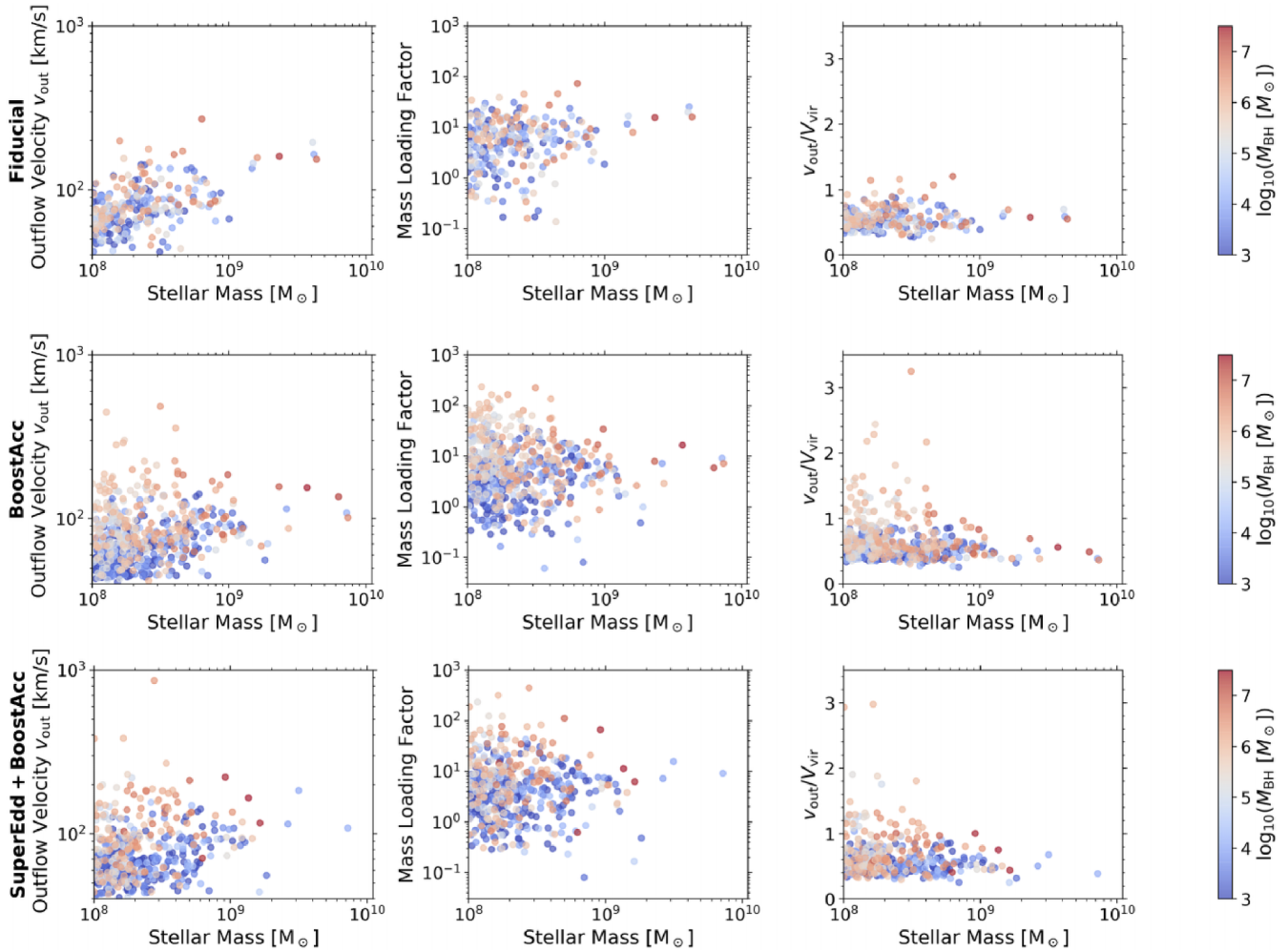

Figure D1. A summary of simulated outflow properties at $z \sim 7.6$ from AESOPICA. The points on each plot are colour-coded according to the black hole mass of the simulated galaxy, with more massive black holes indicated by the red points. Rows, from top to bottom: results from *Fiducial*, *BoostAcc*, and *SuperEdd+BoostAcc* variations on the main AESOPICA simulations. Columns, from left to right: the simulated outflow velocity, mass-loading factor, and v_{out}/v_{vir}. Note that following S. Koudmani et al. (2022), we use the virial velocity as proxy for the escape velocity. Boosted AGN accretion leads to significantly stronger outflows in low-mass galaxies.

This paper has been typeset from a TEX/LATEX file prepared by the author.

Downloaded from https://academic.oup.com/mnras/article/546/3/stag094/8426291 by guest on 31 March 2026

© The Author(s) 2026.
Published by Oxford University Press on behalf of Royal Astronomical Society. This is an Open Access article distributed under the terms of the Creative Commons Attribution License (https://creativecommons.org/licenses/by/4.0/), which permits unrestricted reuse, distribution, and reproduction in any medium, provided the original work is properly cited.